Vision is Required for Cell Type Specification in the Visual Cortex

Sarah Cheng[1,2*], Salwan Butrus[3*], Vincent Xu[1], Srikant Sagireddy[3], Liming Tan[1], Karthik Shekhar[3,4^], and S. Lawrence Zipursky[1^]

Author Affiliations:

1. Department of Biological Chemistry, Howard Hughes Medical Institute, David Geffen School of Medicine, University of California, Los Angeles, Los Angeles, CA 90095, USA

2. Department of Ophthalmology, Stein Eye Institute, David Geffen School of Medicine, University of California, Los Angeles, Los Angeles, CA, 90095, USA.

3. Department of Chemical and Biomolecular Engineering; Helen Wills Neuroscience Institute; California Institute for Quantitative Biosciences, QB3, University of California, Berkeley, CA, USA 94720

4. Faculty Scientist, Biological Systems and Engineering Division, Lawrence Berkeley National Laboratory, CA, USA 94720

*These authors contributed equally

^Correspondence

Karthik Shekhar (kshekhar@berkeley.edu)
S. Lawrence Zipursky (lzipursky@mednet.ucla.edu)

ABSTRACT

The role of postnatal experience in mammalian cortical development, while long appreciated, is poorly understood at the resolution of cell types. To explore this issue, we used single-nucleus RNA-sequencing to profile the mouse visual cortex at different times in postnatal life with and without visual experience. The identities of glutamatergic cell types in upper layers (L) (L2/3/4) were established following eye opening. L2/3 cell types formed a spatial continuum, defined by the graded expression of ~200 genes that included candidates associated with synapse formation and axon projection specificity. These patterns required visual input for both their establishment and maintenance. By contrast to upper-layer glutamatergic neurons, the remaining neuronal and non-neuronal types were established in a vision-independent fashion. Our results demonstrate that vision acts preferentially in the specification of cortical cell types and provide a framework for exploring experience-dependent cortical development at the cellular and molecular level.

Keywords: single-cell RNA-seq, visual cortex, cell types, critical period, layer 2/3

INTRODUCTION

The formation of neural circuitry in the mammalian cortex relies on the interaction of the developing postnatal animal with its environment. Cortical circuits comprise diverse cell types and a network of complex patterns of synaptic connections between them[1,2]. The development of this circuitry relies on genetically hard-wired mechanisms mediated by cell recognition molecules and sensory-independent neural activity[3-8]. During postnatal development, experience-dependent processes are required for maturation of this circuitry[5,9-12]. How the interplay between genetics and experience at this last stage of circuit assembly regulates the development of cortical cell types and the connections between them is not well understood.

The influence of experience on cortical circuitry in the primary visual cortex (V1) is accessible to molecular and genetic analysis in the mouse[9]. Neural circuitry in L2/3/4 is patterned by vision[13,14]. Mice open their eyes around postnatal day (P)14 and the critical period for sensitivity to visual experience in V1 (i.e., the effects of ocular dominance plasticity) begins several days after eye opening (~P21) and continues through ~P35[13,15]. Visual input during this period is necessary to tune and maintain the receptive field properties of both binocular and monocular neurons, and for the development of the neural circuitry underlying binocular vision[5,13-17]. More recent studies have demonstrated a role for vision in regulating V1 circuitry commencing at eye opening[18,19]. In sum, visual experience during the first three weeks following eye opening is required for development of the visual cortex.

Recent advances in single-cell transcriptomics have uncovered a vast diversity of neuronal cell types in the adult mouse V1[1,20,21]. Previous work discovered changes in vision-dependent gene expression in V1 during the critical period[22,23]. These studies highlighted the role of specific signaling pathways in mediating vision-dependent sculpting of circuitry and the expression and function of specific genes regulating development during the critical period. The role of postnatal experience, however, has not been explored in the context of the extensive diversity of neuron types in V1. This level of

resolution is essential for understanding how activity regulates the structure and function of cortical circuitry.

Here we leverage single-cell transcriptomics to uncover experience-dependent regulatory mechanisms at the level of individual cell types. We used single-nucleus RNA-seq to construct a developmental atlas of cell types in V1 during postnatal life, spanning early stages of synaptogenesis (P8) through the closure of the classical critical period (P38)[15,24-26] in both normal and dark-reared animals. We discovered that glutamatergic (excitatory) cell type identities in superficial layers (L2/3/4) were specified after eye opening. L2/3 neuronal types formed a transcriptomic continuum through the graded expression of ~200 genes and were organized as sublayers. The establishment and maintenance of L2/3 cell types required vision. By contrast, the molecular identities of all GABAergic (inhibitory) neuron types and glutamatergic neuron types within the deeper cortical layers (L5 and 6) were specified prior to P8 and did not require vision for their maturation. Thus, experience during early postnatal development specifies a distinct subset of glutamatergic neuron types in the visual cortex. These findings raise the intriguing possibility that plasticity in the developing postnatal mammalian brain occurs at the level of cell type specification as a consequence of interactions between genetic programs and experience.

RESULTS

Transcriptional profiling of mouse V1 development using single-nucleus RNA-seq

To survey the transcriptomic diversity and maturation of cells in V1, we used droplet-based single-nucleus (sn) RNA-seq to profile this region during postnatal development in normally reared mice (**Figures 1A** and **S1D**). We collected samples from six postnatal time points: P8, P14, P17, P21, P28 and P38 (**Figure 1B**). The first three time points are prior to the classical critical period for ocular dominance plasticity, with synaptogenesis occurring between P8 and eye-opening (P14)[25,26] (**Figures S1A-C**). The final three timepoints cover the critical period of ocular dominance plasticity [13,14,16] including its start (P21), peak (P28), and closure (P38).

Data from each timepoint consisted of four single-nuclei library replicates, each derived from cells collected from multiple mice (**Methods**). The resulting gene expression matrices were filtered to remove low-quality cells and doublets[27], as well as cells with a high proportion of mitochondrial transcripts (>1%). In total, we obtained 144,725 high-quality nuclear transcriptomes across the six time points (**Figures S1D-H**).

A postnatal developmental atlas of V1 cell classes, subclasses, and types

We used dimensionality reduction and clustering to derive a developmental taxonomy consisting of cell classes, subclasses, and types[28-30] at each of the six time points (**Figures 1C, D** and **S1D; Methods**). Cell classes consisted of glutamatergic neurons (n=92,856; 3176 genes/cell detected on average), GABAergic neurons (n=13,374*;* 2966 genes/cell), and non-neuronal cells (n=38,495; 1549 genes/cell) identified by canonical markers (**Figure S1I** and **Table S1**)[1,20,21]. The relative proportions of the three cell classes were consistent across biological replicates (data not shown).

Glutamatergic cells separated into eight subclasses within the four cortical layers - L2/3, L4, L5IT, L5NP, L5PT, L6CT, L6IT, and L6b (**Figures 2A, B**). We also identified six GABAergic subclasses, which included the four well-known subclasses defined by the

selective expression of *Pvalb*, *Sst*, *Vip*, and *Lamp5*[28] and two smaller subclasses that selectively expressed the genes *Stac* and *Frem1*. Non-neuronal cells included oligodendrocytes, oligodendrocyte precursor cells, astrocytes, vascular and leptomeningeal cells, endothelial cells, and microglia (**Figure 1D**). Similar results were obtained using an alternative computational pipeline[31] (**Figure S1K**). We found a tight correspondence between the transcriptome-wide gene signatures that defined developing subclasses in our dataset and the subclasses identified in a recent survey of the adult mouse cortex[20] (**Figure S1J**).

The relative proportions of most neuronal subclasses were stable over time (**Figures 2C** and **S1L**), although proportions of non-neuronal subclasses varied (**Figure S1M**)**.** This suggests that the neuronal subclass composition of V1 is established before P8, our earliest time point. We also identified novel subclass-specific markers (**Figures 2B** and **S2A-E**). This included *Ccbe1* (collagen and calcium-binding EGF domain-containing protein 1), which is specific for L2/3 glutamatergic neurons throughout development (**Figures 2D** and **S2A-C**).

We performed dimensionality reduction and clustering for each class at each age separately. We henceforth refer to transcriptomically distinct clusters as types. The eight glutamatergic subclasses separated into 14-16 types, the six GABAergic subclasses separated into 14-15 types, and the six non-neuronal subclasses separated into 9-11 types depending upon age (**Figure 1D**) (**Methods**). Post-hoc differential expression analysis identified robust cell type-specific markers at each age (**Figures S3A-C**).

Transcriptomic identities of L2/3 neuron types are established after eye opening

While the number of cell types within each class was similar at each age, it was not immediately clear how types identified at different ages were related to each other. Using transcriptomic similarity as a proxy for temporal relationships, we tracked the postnatal maturation of types within each class using a supervised classification framework (**Methods**).

We observed striking subclass-specific differences in the maturation of glutamatergic neuron types (**Figure 2E**). Lower-layer neuron types (L5 and L6) tightly corresponded throughout the time course, indicating that these types are established prior to P8, and maintained. Conversely, upper-layer neuron types (L2/3 and L4) exhibited poor correspondences, suggesting gradual specification. Within L2/3, two neuron types at P8 and P14 matured into three types that gradually became better defined with age (see below). By contrast, differences in the maturational patterns of GABAergic and non-neuronal subclasses were less pronounced (**Figures S2F-L, Methods**).

These subclass-specific differences in the timing of glutamatergic neuron type development are supported by four quantitative observations: (**1**) L5/6 types at different ages could be related in a 1:1 fashion with each other while L2/3/4 types could not be. These differences were based on the Adjusted Rand index (ARI), a measure of transcriptomic correspondence between two sets of clusters (**Figure 2F**). Furthermore, the clustering results for L2/3 and L4 were more sensitive (*P<0.0001,* one-way ANOVA) to changes in the resolution parameter than for L5 and L6 (**Figure 2G**); (**2**) Differentially expressed genes that distinguished L2/3 and L4 neuron types varied with age, whereas those that defined L5 and L6 neuron types were stable (**Figures S3D-G**); (**3**) The transcriptomic separation among L2/3 and L4 types was lower than that among L5 and L6 types, GABAergic types, and non-neuronal types at all ages (**Figures S2J-L**); and (**4**) The relative frequency of L2/3 and L4 types varied over time (see below). By contrast, the relative proportions of the ten L5 and L6 types, the smallest of which was present at an overall frequency of 1%, were stable throughout the time course. Together, these results suggest that within glutamatergic neurons of V1, transcriptomic specification of types within upper-layer subclasses (L2/3 and L4) occurs later than types in lower-layer subclasses (L5 and L6).

<u>L2/3 neuron types are spatially segregated</u>

We classified L2/3 glutamatergic neurons into three types (A, B, and C) beginning at P17, the first time point assessed after the onset of vision at P14 (**Figure 3A**). These were visualized in tissue using *in situ* hybridization for marker genes *Cdh13*, *Trpc6*, and *Chrm2* for types L2/3_A, L2/3_B, and L2/3_C, respectively (**Figures 3B-D**). Cells expressing the three transcripts were organized into sublayers that became more pronounced with age: L2/3_A close to the pia, L2/3_C bordering L4, and L2/3_B in between (**Figures 3D, E**). These sublayers lacked sharp boundaries, mirroring their continuous transcriptomic arrangement *in silico* (see below).

Prior to the onset of vision (P8 and P14), however, only two transcriptomic types were resolved. We denote these AB and BC. AB and BC were organized as two sublayers based on their differential expression of *Cdh13* and *Chrm2* (**Figures 3C** and **S4A-E**). In contrast, the B marker *Trpc6* was weakly expressed in cells scattered throughout L2/3 at these early stages (**Figures 3B-C, E-H,** and **S4C, E**). Multiple A-, B-, and C-specific markers were not expressed before P14 and only appeared at later stages (**Figure S3D**). Thus, we infer that the L2/3 glutamatergic types A, B, and C arise from AB and BC types following the onset of vision (**Figure 2E** and **Methods**).

Vision is necessary for establishing and maintaining L2/3 neuron type identity

The emergence of three L2/3 neuron types following eye-opening prompted us to explore the role of vision in defining cell types. It is well established that vision is required for the development of cortical circuitry during the critical period for ocular dominance plasticity (P21-P38)[13,15]. We used snRNA-seq to profile V1 in animals that were dark-reared from P21 to P28 and P21 to P38. For brevity, these experiments are referred to as P28DR and P38DR, respectively (DR = dark rearing). We also profiled animals that were exposed to 8 hours of ambient light after dark-rearing from P21-P28 to assess the impact of visual stimulation following prolonged deprivation (**Figure 4A**). We refer to this experiment as P28DL (DL = dark-light adaptation). In total, we recovered 77,150 high-quality nuclei across these three experiments and identified classes, subclasses, and types using the

same computational pipeline applied to the normally reared (NR) samples (**Figure 4B** and **Methods**).

Dark rearing significantly affected neuron type identities of L2/3 and L4, but not L5 and L6, glutamatergic neurons (**Figures 4C-E** and **S5D-F**). Furthermore, dark-rearing neither altered the gene expression patterns that defined subclasses nor those defining GABAergic and non-neuronal cell types (**Figures S5A-C**). Thus, vision selectively influences transcriptomic profiles of upper-layer glutamatergic cell types.

The effect of dark rearing was particularly striking in L2/3. The L2/3 clusters observed in dark-reared mice poorly resembled the three types in normally reared animals, and the expression patterns of cell type-specific marker genes were disrupted (**Figure 4C,D**). By contrast to the three sublayers highlighted by *Cdh13, Trpc6,* and *Chrm2* expression in L2/3 in normally reared mice, only two sublayers were observed in dark-reared mice. Notably, there was a sharp decrease in *Trpc6*-expressing cells (**Figure 4F-J**), consistent with snRNA-seq data (**Figure 4D**). This was not simply a loss of one cell type, however, but a global disruption of gene expression patterns throughout L2/3 (see below, **Figure 6**). The two-layered pattern was more prominent in dark-reared animals at P38 compared to P28 (**Figures 4G-I** and **S5H-I**). Thus, in the absence of vision, the expression patterns of these markers were similar to those prior to the onset of vision (see panels P8 and P14 in **Figure 3E**).

The loss of cell type identity in animals deprived of light during the first half of the critical period was partially reversible. L2/3 transcriptomic clusters in mice exposed to 8 hours of ambient light after dark rearing between P21-P28 showed a marked recovery of gene expression patterns observed in normally reared animals (**Figures 4C-D** and **S5G**). In addition, the layered arrangement of *Cdh13*-, *Trpc6*- and *Chrm2*-expressing cells in these animals was also shifted towards that observed in normally reared animals (**Figures 4F-J** and **S5H-I**). These results demonstrate that vision is needed to maintain the transcriptomic and spatial identities of L2/3 cell types.

As the spatial expression of cell type markers in the absence of vision and at eye opening were similar, we set out to assess whether vision was not only necessary to maintain cell types, but also required for their establishment. To test this, we dark-reared mice from P8 to P17 (**Figure 5A**) and assessed the expression patterns of *Cdh13*, *Trpc6* and *Chrm2* in tissue sections. These mice had two, instead of three, sublayers within L2/3, similar to P8 and P14 normally-reared animals (**Figures 5B-D**). The most dramatic change was the reduced frequency of the *Trpc6*-expressing cells in mice with no visual experience (**Figure 5E**). This was not a general effect on glutamatergic cell types, as the relative proportions of L5 neuron types were insensitive to changes in visual experience (**Figure 5F**). In summary, these results show that vision acts selectively in L2/3 to establish and maintain cell types.

Continuous variation of L2/3 neuron types is shaped by vision

The sublayers corresponding to types A, B, and C in L2/3 were partially overlapping, mirroring the continuous arrangement of their transcriptomes (see **Figures 3A, E**). We observed that more than 70% of the 285 differentially expressed genes among the L2/3 types in normally reared mice exhibited graded, rather than digital, differences (**Figures 6A** and **S6A, B)**. In dark-reared mice, these genes were no longer expressed in a graded fashion between the L2/3 clusters, although their overall (i.e., bulk) expression levels were unaltered (**Figures S6C, D**). These gradients were partially restored by brief exposure to ambient light during the critical period (**Figure 6A**). Thus, vision increases expression in some cells and decreases it in others, contributing to the continuous variation of L2/3 cell types.

Several genes exhibiting graded expression were related to functional differences between cell types. For example, two sets of markers (e.g., *Grm1, Cntn5* and *Kcnh5, Astn2*) are associated with L2/3 glutamatergic neurons forming circuits with distinct functions and axon projection specificities to higher visual areas (**Figures 6B, C** and **S6E**)[32,33]. Other gradient genes are associated with synapse formation (e.g., *Tenm1, Cbln2*)[34].

Two genes encoding a positive (*Igsf9b*) and a negative regulator (*Mdga1*) of inhibitory synapses are particularly interesting as they are expressed in anti-parallel gradients along the depth of L2/3 (see **Figure 6A**). Furthermore, *Igsf9b* expression levels are vision-dependent and increase during the critical period (**Figures 6D, E**, and **S6F**). IGSF9B is an immunoglobulin superfamily protein that engages in homophilic adhesion between opposing synaptic membranes and promotes Neuroligin2 (NLG2)-dependent inhibitory synapse formation[35,36] (**Figure 6D**). MDGA1, another immunoglobulin superfamily protein, inhibits inhibitory synapses through direct binding in *cis* to NLG2 and is expressed in a complementary spatial pattern to *Igsf9b* with the onset of vision (**Figure 6E**)[37,38]. *Mdga1* expression in L2/3 decreased during the critical period (**Figure S6F**). By regarding the reduced dimensional representation of cells in UMAP as “pseudo” spatial coordinates, we were also able to qualitatively recover these spatiotemporal patterns *in silico* (**Figure 6F; Methods**). In contrast to *Mdga1* and *Igsf9b*, the level of *Nlgn2* expression remained constant throughout development and was uniformly distributed throughout L2/3 (data not shown). Thus, these patterns would contribute to a gradient of NLG2-dependent inhibitory synapses onto L2/3 glutamatergic neurons with increased inhibition in deeper sublayers.

The spatiotemporal changes in expression of these modulators of inhibitory synapses after eye opening were influenced by vision. Dark-rearing during the critical period decreased *Igsf9b* expression and disrupted its graded expression in L2/3 neurons (**Figures 6G-I** and **S6G, H**). *Igsf9b* expression levels were recovered when dark reared animals were briefly exposed to ambient light for 8hrs (**Figure 6G-I** and **S6G, H**). By contrast, the influence of vision on *Mdga1* expression was modest. These changes in gene expression would tend to promote inhibitory synapse formation preferentially in cell types in lower sublayers in a vision-dependent manner. The degree to which the spatiotemporal distribution and light-dependent expression of these cell surface proteins regulates inhibitory synapses in L2/3 will be addressed through genetic analysis in future studies.

Taken together these data indicate that vision is required to maintain spatiotemporal gene expression gradients that underlie continuous L2/3 cell type identity.

DISCUSSION

It has long been known that visual experience is necessary for the establishment of neural circuitry in the primary visual cortex. Here, we explored this process at the molecular level by profiling the transcriptomes of cells in V1 and examining the role of vision in cell type specification. We discovered that the establishment and maintenance of glutamatergic neuronal cell types in upper layers, particularly in L2/3, and their sublayer organization required vision. By contrast, the transcriptomic identities of the remaining cell types were unaffected by visual deprivation. These findings demonstrate that visual experience is essential for the development of specific cell types in the visual cortex.

A postnatal developmental atlas of mouse V1

Our developmental atlas of mouse V1 comprised over 220,000 nuclear transcriptomes spanning six postnatal ages and three light-rearing conditions. Several features of this dataset enabled us to identify biological signals that were robust and reproducible. First, we identified a similar number of transcriptomic clusters at all six ages, which were collected and processed separately. For all clusters, transcriptomic identities and relative proportions were comparable between independent samples, consistent with these being bona fide cell types. Second, computational inference of transcriptomic maturation showed that the GABAergic, deep-layer glutamatergic, and non-neuronal cell types were present prior to eye opening and remained largely unchanged through the critical period, whether animals were reared in a normal dark/light cycle or in the dark. Third, these stable cell types served as important “negative controls” that enabled us to identify the minority of cell types among the upper layer glutamatergic neurons that were specified following eye opening, and whose transcriptomic identities were profoundly influenced by vision. Fourth, we identified novel cell type markers that enabled us to uncover the arrangement of L2/3 cell types in sublayers **(**see **Figures 3B-D)**. And finally, the developmental atlas

served as a foundation to investigate vision-dependent maturational changes at cell type resolution.

Continuous variation in L2/3 identity and sublayer arrangement

Although unsupervised clustering defined three predominant glutamatergic neuronal types in L2/3, the gene expression differences between them were graded, giving rise to continuous variation in transcriptomic identity (**Figures 6A** and **S6A**). This continuous variation *in silico* was seen as a spatially graded sublayered arrangement in L2/3 via FISH. Continuous variation of cell type identity has been reported in other regions of the mammalian brain[39-42]. This contrasts the transcriptomic features of neurons in the fly brain and mammalian retina where cell types exhibit molecularly discrete identities, even for highly related neurons[43-45]. Circuits comprising continuously variable cell types may provide more flexible computational properties for information processing [40].

A subset of the genes that exhibited graded variation among L2/3 cell types were associated with neurons projecting to different higher visual areas (**Figures 6B-C**)[32,33,46]. Thus, L2/3 neurons may form functionally distinct circuits preferentially in lower and upper sublayers, respectively. Other L2/3 neurons project to different higher visual areas or combinations of them[33,46]. These findings raise the intriguing notion that the multiple subnetworks of cortical circuitry comprising L2/3[47] may be arranged in a sublayered fashion. Sublayer organization may facilitate preferential connectivity between neurons of the same type. It may also provide an efficient strategy to organize the axon projections from the same glutamatergic types to the same higher visual areas and recurrent connections from these back to their appropriate sublayers[5].

The establishment and maintenance of L2/3 neuron types require vision

Transcriptomic type identity emerges gradually in L2/3 glutamatergic neurons during postnatal development. In previous functional studies, we uncovered marked instability of their receptive field properties during the same period. As vision plays an important

role in improving and stabilizing the functional properties of these neurons[14,19], we set out to assess whether specification of L2/3 glutamatergic cell types also relied on vision.

We discovered that vision is required for the establishment and maintenance of L2/3 glutamatergic cell type identities through the regulation of cell type-specific graded expression of many genes. This is not a general feature of glutamatergic cell type development in the visual cortex, as glutamatergic cell type identity in deeper layers of V1 is independent of vision. Further, even within L2/3 glutamatergic neurons, visual deprivation abrogated the expression patterns of these genes without disrupting their average expression levels. This highlights the importance of examining changes in gene expression at the level of specific cell types.

Our findings broaden the role of neural activity in regulating cellular development. It is well established that neural activity regulates gene expression[21,48,49]. Recent studies have shown that different patterns of neural activity lead to qualitative differences in gene expression[50]. For instance, distinct patterns of neural activity in different olfactory sensory neurons promote expression of different recognition molecules. These, in turn, regulate the specificity of their connections[51]. Previous studies have identified specific genes contributing to activity-dependent changes in circuitry during the critical period[52]. To our knowledge, however, previous studies have not addressed the role of experience in establishing and maintaining cell types in the mammalian brain. It seems likely that the role of experience in regulating cell type identity will extend to other regions of the cortex beyond V1[53].

<u>The vision-dependent expression of genes regulating inhibitory synapses</u>

Genes expressed in a graded fashion among L2/3 types were functionally diverse. They included transcription factors, cell recognition molecules, synaptic adhesion proteins, and growth factors, among others. These could contribute to the co-evolution of circuitry and cell type specification in sublayer-specific ways. Additionally, we observed dramatic changes between eye opening and P17 in the expression patterns of *Mdga1* and *Igsf9b*,

two genes encoding Ig superfamily proteins that modulate inhibitory synapse formation (**Figure 6D**). These patterns would promote a graded increase in NLG2-dependent inhibition increasing from the top of L2/3 towards the boundary between L2/3 and L4. This is consistent with the importance of inhibition in maturation of cortical circuitry during the critical period[9,11,54,55]. Different levels of inhibition may alter patterns of activity in different sublayers. These, in turn, may contribute to cell type diversification along the depth of L2/3 in concert with, and contributing to, functional circuit maturation in different sublayers.

Cell types vs. cell states

A common question in single-cell analysis is whether transcriptomically identified clusters represent stable cell types or transient cell states[56]. In the context of our dataset, while distinctions at the class and subclass level are unequivocal, one might be tempted to ask whether clusters within a subclass (e.g., L2/3_A, L2/3_B, or L2/3_C) represent transitory states that a single neuron could cycle between. This is unlikely for two reasons. First, some 300 genes, which do not include known immediate/early response genes[21], are differentially expressed robustly among L2/3 clusters. The magnitude of these distinctions is comparable to those observed between closely related, but distinct cell types defined by their different morphologies and connectivity in other parts of the mouse CNS[57,58]. Second, the expression patterns of these genes are reflected in the sublayered organization of the A, B, and C types in L2/3, as we have shown by FISH using *Cdh13, Trpc6, Chrm2, Mdga1,* and *Igsf9b* as markers across multiple time points during development. It is difficult to conceive of postmitotic neurons cycling through transitory cell states producing these robust and stable spatial patterns.

Concluding Remarks

Experience plays a key role in the development of neural circuitry in mammals, impacting neural processes from sensory perception to cognition. The importance of the work we describe here lies in the surprising discovery that sensory experience plays a profound

and selective role in generating a continuum of glutamatergic cell types in L2/3. We envision a complex interplay between genetic programs and experience in establishing neural circuitry. Here, local circuitry within V1, recurrent inputs from higher visual areas, and inputs from other brain areas may, alone or in combination, sculpt cell type-specific transcriptomes and circuitry gradually and reiteratively within different sublayers. These changes, in turn, would alter the circuit properties of neurons (e.g., their patterns of connections or synaptic function) leading to the establishment of multiple sublayer-specific networks of circuits with distinct functional properties.

Our findings raise the important possibility that experience-dependent cell type specification is a general phenomenon in mammalian brain development. Understanding how the interplay between circuit function, cell type specification, and experience sculpts circuitry will rely on integrating multiple levels of analysis, including connectomics, transcriptomics and proteomics, physiology, genetics, and computational modeling.

ACKNOWLEDGEMENTS

The authors would like to thank Maria del Carmen Diaz de la Loza for illustrations. Select images were made using BioRender. We thank Michael Mashock and Xinmin Li from UCLA Technology Center for Genomics and Bioinformatics for assistance with scRNA-seq. We also thank Andrew Elkins and Drs. Damon Polioudakis and Dan Geschwind for advice and help at early stages in this project. We are grateful to Drs. Weize Hong, Jonathan Flint, Emile Marcus, Dario Ringach, Joshua Sanes, and Joshua Trachtenberg, and members of the Shekhar and Zipursky labs for critical feedback. We thank Drs., Nathan Gouwens, Clay Reid, Staci Sorensen, Bosiljka Tasic, Zizhen Yao, and Hongkui Zeng for helpful discussions and sharing unpublished data. This work was supported by the Stein Eye Institute EyeSTAR program (S.C.), NSF Graduate Research Fellowship (grant DGE1752814 to S.B.), an NIH grant (R00EY028625 to K.S.), a grant from the W.M. Keck Foundation to S.L.Z, and startup funds from the University of California, Berkeley (K.S). S.L.Z. is an investigator of the Howard Hughes Medical Institute.

AUTHOR CONTRIBUTIONS

S.C., L.T., and S.L.Z conceived the project and designed snRNA-seq experiments. S.B. and K.S. conceived and designed the computational methods for transcriptomic analysis. S.C. carried out snRNA-seq and initial bioinformatic analysis. S.B. and S.S. performed the transcriptomic analysis. S.C. and V.X designed and carried out FISH experiments. K.S. and S.L.Z provided supervision and acquired funding. S.C, S.B., K.S. and S.L.Z analyzed the data and wrote the paper.

DECLARATION OF INTERESTS

The authors declare no competing interests

METHODS

Animals

Mouse breeding and husbandry procedures were carried out in accordance with UCLA's animal care and use committee protocol number 2009-031-31A, at University of California, Los Angeles. Mice were given food and water *ad libitum*, and lived in a 12-hr day/night cycle with up to four adult animals per cage. Only virgin male C57BL/6J wild-type mice were used in this study.

Visual deprivation experiments

Mice that were dark-reared were done so in a box covered from inside and outside with black rubberized fabric (ThorLabs Cat# BK5) for 7-17 days (P21-P28 or P21-P38) or 9 days (P8-P17) before being euthanized. The dark box was only opened with red light on in the room (mice cannot perceive red light). Mice that were dark-light reared were first dark reared for 7 days from P21 to P28 in the dark, and then transferred back to the mouse room to receive 8 hours of ambient light prior to euthanasia.

V1 dissection to obtain single nuclei

Normally-reared mice were dissected at P8, P14, P17, P21, P28, and P38. Isoflurane was used for anesthetization and mice were euthanized by cervical dislocation. Dark-reared mice were dissected at P28 and P38. Dark-light reared mice were dissected at P28 after exposure to 8 hr ambient light. For each age or condition group, 30 mice were dissected: 15 for each biological replicate of single-nucleus(sn) RNA-sequencing. Mice were anesthetized in an isoflurane chamber, decapitated, and the brain was immediately removed and submerged in Hibernate A (BrainBits Cat# HACA). While the dissection was aimed to target V1b, the region enriched for binocular neurons, due to the small size of this region, the dissection invariably captured neighboring V1 tissue. Therefore, we refer to the tissue as V1. Extracted brains were placed on a metal mold and the slice containing V1 was isolated by inserting one blade 0.5 mm posterior to the lambdoid suture and a second blade 1.5 mm further anterior (2 spaces on the mold). This slice was removed and lowered to Hibernate A in a 60cc petri dish, which was placed on a ruler under a

dissecting microscope. The midline was aligned with the ruler and the first cut was bilaterally 3.2 mm out from the midline. The second cut was 1 mm medial to the first cut. The cortex was peeled off the underlying white matter. The V1 piece with a total of 1 mm cortex depth by 1.5 mm thickness was transferred to a dish containing 600 µl of RNAlater (Thermo Fisher Cat# AM7020) and kept on ice until dissections were complete. Dissected tissues were then kept in RNAlater at 4°C overnight and transferred to -20°C the next day. Tissue was stored this way for up to 1 month prior to being processed for snRNA-seq.

Droplet-based single-nucleus(sn) RNA-sequencing

For each biological replicate, dissected V1 regions from 15 mice were removed from RNAlater, weighed, then chopped with a small blade on a cleaned slide on top of a cooling cube. Tissue was then transferred to a dounce homogenizer chilled to 4°C and denounced slowly 30 times with a tight pestle in 1 ml of homogenization buffer containing 250mM Sucrose, 150mM KCl, 30mM $MgCl_2$, 60mM Tris pH 8, 1 µM DTT, 0.5x protease inhibitor (Sigma-Aldrich Cat# 11697498001**)**, 0.2 U/µl RNase inhibitor, and 0.1%TritonX. All solutions were made with RNase-free H_2O. Each sample was filtered through a 40 µm cell strainer and then centrifuged at 1000g for 10 minutes at 4°C. The pellet was resuspended in the homogenization buffer and an equal volume of 50% iodixanol was added to the resuspended pellet to create 25% iodixanol and nuclei mix. This mix was layered upon 29% iodixanol and spun at 13,500g for 20 minutes at 4°C. The supernatant was removed and the pellet was washed in a buffer containing 0.2 U/µl RNAse inhibitor, PBS (137 mM NaCl, 2.7 mM KCl, 8 mM Na_2HPO_4, and 2 mM KH_2PO_4, pH 7.4), 1% bovine serum albumin, and then filtered over a 40 µm filter and centrifuged at 500g for 10 minutes at 4°C. The pellet was resuspended and filtered with two more 40 µm filters, cells counted on a hemocytometer and then diluted to 700-1200 nuclei/mm^3. Nuclei were re-counted on a 10X automated cell counter. Nuclei were further diluted to the optimal concentration to target capturing 8000 cells per channel.

Nuclei from each biological replicate were split into two and run separately on two channels of 10X v3, targeting 8,000 cells per channel. We refer to these as library

replicates. For each experiment, we performed two biological replicates towards a total of four library replicates. The two biological replicates were processed on different days. Sequencing was performed using the Illumina NovaSeq™ 6000 Sequencing System (S2) to a depth of ~30,000 reads per cell. All library preparation and sequencing were performed at the UCLA's Technology Center for Genomics & Bioinformatics (TCBG) core.

Single-molecule fluorescent *in situ* hybridization (smFISH)

C57/BL6J mice were anesthetized in isoflurane at ages ranging from P8 to P38 and then perfused transcardially with heparinized PBS followed by 4% paraformaldehyde (PFA) diluted in PBS and adjusted to pH 7.4. Following perfusion, the brains were collected and postfixed for 24h at 4°C in 4% PFA, and then cryoprotected sequentially in 10%, 20%, and 30% sucrose in PBS solution until the brain sank. Brains were then frozen in OCT using a methylbutane and dry ice bath and stored at -80°C until time of sectioning. Brains were cut into 15 µm thick coronal sections at -22/-20°C using a cryostat (Leica CM 1950) and single sections were collected in a charged microscope slide in ascending order from the frontal to the occipital region starting in V1. For localization of the visual cortex V1 and binocular zone of V1, coordinates from [60] were used. Sections were stored at -80°C until further processing. For all FISH experiments, coronal sections were selected to be from a similar anatomical region within V1 when comparing conditions or ages.

Multiplex FISH was performed following ACD Biology's Multiplex RNAscope v2 assay (Advanced Cell Diagnostics, cat# 323110). Briefly, thawed sections were baked at 60°C, post-fixed for 1 hr at 4°C in 4% PFA, and then dehydrated in sequential ethanol treatments followed by H_2O_2 permeabilization and target retrieval. Protease III treatment was used, then application of probes and sequential amplification and fluorophore development fluorophores (Akoya Biosciences cat# FP1487001KT, FP1488001K, FP1497001KT). Slides were counterstained with 1 ug/ml 4,6-diamidino-2-pheenylindole (DAPI, Sigma cat #D9542) and mounted with Prolong Gold (Thermo Fisher Scientific cat# P36930). RNAscope probes used include: *Igsf9b* (cat# 832171-C3), *Mdga1* (cat#546411, 546411-C2), *Nlgn2* (cat# 406681). Cdh13 (cat # 443251-C3), *Chrm2* (cat # 495311-C2), *Deptor* (cat #481561 - C3), *Gad1* (cat3 400951-C2), *Slc17a7* (cat# 416631-C2, 416631, 416631-

C3), *Trpc6* (cat# 442951), *Tshz2* (cat# 431061-C1). Each time point or condition had three to four biological replicates comprising brain sections from different mice. NR mice at P8, P14, P17, P21, P28, and P38, DR mice at P17, P28, and P38, and DL mice at P28 were used.

Immunolabeling for synaptic markers

Immunolabeling for VGLUT1 and GAD65 was performed on perfusion-fixed brains that underwent the same preparation as for smFISH. Brains were sectioned to 15 µm sections. Sections were then incubated for 24 hr with anti-VGLUT1 (guinea pig polyclonal Millipore Sigma Cat# AB5905) and anti-GAD65 (mouse monoclonal Millipore Sigma Cat#MAB3521R) diluted 1:500 in blocking solution (10% NGS in 0.3% PBST), washed 3x times in PBS, and then incubated for 2 hr with goat anti-mouse 488 (Invitrogen Cat# A11029) and goat anti-guinea pig 568 (Invitrogen Cat#A21244) both diluted 1:500 in blocking solution.

Confocal imaging

Images were acquired on a Zeiss 880 confocal microscope at 20X and 40X magnification. Each image was 1024 pixels x 1024 pixels in size. For 20X and 40X images, this corresponded to a 0.4 µm x 0.4 µm and 0.2 µm x 0.2 µm coverage per frame, respectively. Vertically tiled 20X images were acquired covering the entire cortex, as well as 40X horizontal tiled images to cover L2/3 only. Z-stacks covered the entire 15 µm section. *Mdga1* and *Ccbe1,* both L2/3 -markers, were used as markers to assess the cortical depth covered by each 40X image. For each 40X frame starting at layer 2, one frame covered the depth of L2/3 based on *Mdga1* and *Ccbe1* signals. For immunolabeling experiments, images were taken using a confocal microscope with 63X magnification, imaged on both sides of the brain in L2/3 of V1 based on anatomical markers. One z-stack comprising 5 optical sections spanned the entire 15 µm section imaged.

Imaging quantification

3D z-stacked images were z-projected on FIJI version 2.1.0/1.53c. The entire z-stack covering the slide was projected into a 2D image with maximum intensity. 20X images

were tiled using DAPI and *Slc17a7* channels (when available) as guides through linear blending to capture the entire cortical thickness. 40X and 63X images were processed as is. Maximum-projected images were entered into CellProfiler using a custom pipeline modified from the original SABER-FISH pipeline [61]. Modifications were made to detect up to four imaging channels [62]. CellProfiler was used to perform nuclear and cell segmentation, as well as puncta counting. Nuclear segmentation was done by using DAPI and cellular segmentation was done by taking a fixed radius of 5 pixels around the nucleus. For downstream computation, nuclear segmentation results were used. Segmented images had nuclear boundaries as well as individual puncta married in an overlay color with original image items in gray. All segmented images were inspected to ensure no aberration in segmentation or puncta calling.

After segmentation and puncta calling, data were analyzed in R using custom scripts to compare nuclear mRNA counts (i.e., number of puncta) between time points and conditions. For cell type experiments, cells were sorted into types based on mRNA counts of marker genes. Briefly, cells were ranked based on their mRNA counts of each gene and visualized as a scatter plot of counts vs. rank. The knee of this plot was located [63]. The mRNA count value at the knee was chosen as the cutoff for cell type assignment. Quantification of protein puncta in immunolabeling experiments also used Cell Profiler by adapting the same pipeline developed to count mRNA puncta.

Computational analysis of single-nucleus transcriptomics data

Alignment and quantification of gene expression

Fastq files with raw reads were processed using Cell Ranger v3.1.0 (10X Genomics) with default parameters. The reference genome and transcriptome used was GRCm38.92 based on Ensembl 92, which was converted to a pre-mRNA reference package by following Cell Ranger guidelines. Each single-nucleus library was processed using the same settings to yield a gene expression matrix (GEM) of mRNA counts across genes (columns) and single nuclei (rows). Each row ID was tagged with the sample name for later batch correction and meta-analysis. We henceforth refer to each nuclear transcriptome as a “cell.”

Initial pre-processing of normally reared samples to define classes, subclasses, and types

This section outlines the initial transcriptomic analysis of data from normally-reared samples. Unless otherwise noted, all analyses were performed in Python using the SCANPY package [64]. The complete computational workflow is illustrated in **Figure S1D**.

1. Raw GEMs from 23 snRNA-seq libraries were combined: 6 ages, 2 biological replicates per age and 2 library replicates per biological replicate except for P38, where one of the technical replicates failed quality metrics at the earliest stage of processing. This resulted in a GEM containing 184,936 cells and 53,801 genes.
2. We then generated scatter plots of the number of transcript molecules in each cell (n_counts), the percent of transcripts derived from mitochondrially encoded genes (percent_mito), and the number of expressed genes (n_genes) to identify outlier cells. Cells that satisfied the following conditions were retained: 700 < n_genes < 6500, percent_mito < 1%, and n_counts < 40,000. Only genes detected in more than 8 cells were retained for further analysis. This resulted in a GEM of 167,384 cells and 30,869 genes.
3. Cells were normalized for library size differences. Transcript counts in each cell were rescaled to sum to 10,000 followed by log-transformation. For clustering and visualization, we followed steps described previously [65]. Briefly, we identified highly variable genes (HVGs), z-scored expression values for each gene, and computed a reduced dimensional representation of the data using principal component analysis (PCA). The top 40 principal components (PCs) were used to compute a nearest-neighbor graph on the cells. The graph was then clustered using the Leiden algorithm [66] and embedded in 2D via the Uniform Manifold Approximation and Projection (UMAP) algorithm [67].

Additional filtering and class assignment

The analysis above yielded 42 clusters (**Figures S1E-F**). Canonical marker genes for cortical classes and subclasses were used to annotate these clusters (**Figure S1G, Table S1**). We then used Scrublet [27] to identify doublets (**Figure S1H**). Clusters that expressed markers of two or more classes or contained more than 50% doublets were labeled

"Ambiguous" (**Figure S1I**). Removal of ambiguous clusters and doublets in the dataset resulted in a GEM containing 147,236 cells by 30,868 genes.

For further analysis, this matrix was subsetted by cell class (glutamatergic neurons, GABAergic neurons, and non-neuronal cells) and age (P8, P14, P17, P21, P28 and P38) into 18 separate GEMs (**Figure S1D**).

Identification of cell types within each class by age

Each of the 18 GEMs were separately clustered using the procedure described above with one modification. Following PCA, we used Harmony [68] to perform batch correction. The nearest-neighbor graph was computed using the top 40 batch-corrected PCs.

Each GEM was then iteratively clustered. We began by clustering cells using the Leiden algorithm, with the resolution parameter fixed at its default value of 1. As before, UMAP was used to visualize the clusters in 2D. Through manual inspection, small clusters with poor quality metrics or ambiguous expression signatures were discarded, likely representing trace contaminants that escaped detection in the earlier steps. The remaining clusters were annotated by subclass based on canonical expression markers (**Table S1, Figure 1D**). Next, we performed a differential expression (DE) analysis between each cluster and other clusters in its subclass. If a cluster did not display unique expression of one or more genes, it was merged with the nearest neighboring cluster in the UMAP embedding as a step to mitigate over-clustering. This DE and merging process was repeated until each cluster had at least one unique molecular signature (**Figures S3A-C**). We refer to the final set of clusters as types.

Workflow for supervised classification analyses

To assess transcriptomic correspondence of clusters across ages or between rearing conditions, we used XGBoost, a gradient boosted decision tree-based classification algorithm [69]. In a typical workflow, we trained an XGBoost (version 1.3.3) classifier to learn subclass or type labels within a "reference" dataset, and used it to classify cells from another, "test" dataset. The correspondences between cluster IDs and classifier-assigned

labels for the test dataset are used to map subclasses or types between datasets. The classification workflow is described in general terms below and applied to various scenarios in subsequent sections.

Let R denote the reference dataset containing N_R cells grouped into r clusters. Let T denote the test dataset containing N_T cells grouped into t clusters. Here, each cell is a normalized and log-transformed gene expression vector $\boldsymbol{u} \in R$ or $\boldsymbol{v} \in T$. The length of $\boldsymbol{u}$ or $\boldsymbol{v}$ equals the number of genes. Based on clustering results, each cell in R or T is assigned a single cluster label, denoted cluster($\boldsymbol{u}$) or cluster($\boldsymbol{v}$). cluster($\boldsymbol{u}$) may be a type or subclass identity, depending on context.

The main steps are as follows:

1. We trained multi-class XGBoost classifiers C_R^0 and C_R^T on R and T independently using all 30,868 genes as features. In each case, the dataset was split into training and validation subsets. For training we randomly sampled 70% of the cells in each cluster, up to a maximum of 700 cells per cluster. The remaining "held-out" cells were used for evaluating classifier performance. Clusters with fewer than 100 cells in the training set were upsampled via bootstrapping to 100 cells in order to improve classifier accuracy for the smaller clusters. Classifiers achieved a 99% accuracy or higher on the validation set. XGBoost parameters were fixed at the following values:
    1. 'Objective': 'multi:softprob'
    2. 'eval_metric': 'mlogloss'
    3. 'Num_class': r (or t)
    4. 'eta': 0.2
    5. 'Max_depth': 6
    6. 'Subsample': 0.6
2. When applied to a test vector $\boldsymbol{c}$, the classifier C_R^0 or C_R^T returns a vector $p = (p_1, p_2, \ldots)$ of length r or t, respectively. Here, p_i represents the probability value of predicted cluster membership within R or T, respectively. These values are used to compute the "softmax" assignment of $\boldsymbol{c}$, such that cluster($\boldsymbol{c}$) = $arg\ max_i\ p_i$ if arg

$max_i\ p_i$ is greater than *1.2*(1/r)* or 1.2**(1/t)*. Otherwise ***c*** is classified as 'Unassigned'.

3. Post training, we identified the set of top 500 genes based on average information gain for each C_R^0 and C_R^T. These gene sets are denoted G_R and G_T.
4. Using the common genes $G = G_R \cap G_T$, we trained another classifier C_R on 70% of the cells in R, following the procedure outlined in 1. As before, the performance of C_R was evaluated on the remaining 30% of the data.
5. Finally, we trained a classifier C_R on 100% of the cells in R. C_R was then applied to each cell $\boldsymbol{v} \in T$ to generate predicted labels cluster($\boldsymbol{v}$).

Comparing transcriptomic signatures of developmental V1 to adult V1/ALM subclasses (Tasic et al., 2018)

We used the aforementioned classification workflow to evaluate the correspondence between V1 subclasses in this work (**Figure 1D**) and those reported in a recent study of the adult V1 and motor cortex (ALM) [20]. We trained a classifier on the V1/ALM subclasses and used it to assign an adult label to each V1 cell collected in this study. A confusion matrix was used to visualize the correspondence between developmental V1 subclasses and V1/ALM subclasses at adulthood (**Figure S1J**). This correspondence served as a proxy to evaluate the overall conservation of subclass-specific transcriptomic signatures across developmental stages (developing vs. adult), RNA source (single-nucleus vs. single-cell), platform (3' droplet-based vs. full-length plate-based), and region (V1 vs. V1/ALM).

Inferring temporal association between V1 types using supervised classification

Relating types across time

The supervised classification workflow was used to relate cell types identified at each pair of consecutive ages within each class (5 x 3 = 15 independent analyses). In each case, the classifier was trained on the older age dataset and applied to each cell in the younger age dataset. Thus, each cortical cell at the younger age possessed two type labels, one identified via clustering of cells at that age and the other based on a classier trained at the next age. Assessing the correspondence between these labels enabled us to link cell

types between consecutive ages (e.g., P8-P14, P14-P17 and so on) and track their maturation across development

Quantification and visualization of cluster correspondence

The correspondences between types throughout development were visualized using Sankey flow diagrams (**Figures 2E**, **S2F-G**). In the case of glutamatergic neurons, for example, inspecting the Sankey flow diagrams revealed that L2/3 and 4 types mapped more diffusely across time than L5 and 6 types, suggesting subclass specific differences in maturation. We quantified such subclass-specific differences using three methods,

(1) We computed the adjusted rand index (ARI) between the cluster labels and classifier-assigned labels. The ARI ranges from 0 and 1, with extremes corresponding to random association and perfect (i.e., 1:1) mapping, respectively. Negative values are possible for the ARI but were not observed in our data. The ARI was computed using the function `sklearn.metrics.adjusted_rand_score()`. ARI values were computed for each pair of consecutive ages (e.g., P8 and P14) within each subclass (e.g., L2/3). ARI differences between glutamatergic subclasses were visualized as bar plots (**Figure 2F**). The analysis was repeated for GABAergic and non-neuronal cells (**Figure S2H-I**).

(2) We computed for each type the F1 score, which is a measure of a classifier's effectiveness at associating cells within a type to their correct type label. Its value ranges from 0 to 1, with extremes corresponding to no association and perfect association between transcriptome and type label, respectively. The F1 score was computed for each type at each time point using the function `sklearn.metrics.f1_score()`. Values were grouped by subclass to visualize differences (**Figures S2J-L**). This analysis showed that in addition to exhibiting poor temporal correspondence, L2/3 and L4 types were also less transcriptomically distinct than L5 and L6 types at any given time point (**Figure**

S2J). Subclasses within GABAergic and non-neuronal cells did not exhibit such striking differences (**Figures S2K-L**).

(3) We assessed the sensitivity of each subclass' clustering results to the clustering resolution parameter of the Leiden algorithm, which controls the number of output clusters. The clustering resolution was increased from 1 to 2. We computed the ARI between the clusters identified at each value of the resolution parameter and the baseline clusters computed at a resolution value of 1. The ARI was computed for the clusters within each subclass at each time point separately. L2/3 and L4 clustering was more sensitive to changes in the resolution parameter than the clustering in L5 and L6 (**Figure 2G**).

Analysis of visual deprivation experiments

Separation of major cell classes

In visual deprivation experiments, snRNA-seq profiles were collected from cortical samples of mice dark-reared from P21-P28 (P28DR), dark-reared from P21-P38, (P38DR) and dark-reared from P21-P28 followed by 8 hours of ambient light stimulation. Overall, 12 GEMs from these three experiments were combined and preprocessed (4 libraries per experiment) using the steps described above for normally reared samples. The numbers of cells prior to pre-processing were 43,234, 36,373 and 31,815 for P28DR, P38DR and P28DL respectively. The final numbers of high-quality cells reported were 24,817, 25,671, and 26,575, respectively.

Comparing DR and DL clusters to NR types using supervised classification

To examine cell type correspondence between visual deprivation and normally reared experiments, we used supervised classification as described above. Classifiers were trained on P28NR and P38NR types, and cells from P28DL, P28DR, and P38DR were mapped to the corresponding NR age. The resulting confusion matrices were visualized as dot plots, and the ARI was computed for types within each subclass (**Figure S5**).

Differential gene expression analysis

Differential expression (DE) was performed in multiple settings to identify genes enriched in specific classes, subclasses, types, or rearing conditions. We used the `scanpy.tl.rank_genes_groups()` function and Wilcoxon rank-sum test in the scanpy package for statistical comparisons [64]. While searching for genes enriched in a particular group of interest, only those expressed in >20% of cells in the tested group were considered.

The results of the DE analyses were used in the following contexts: (1) To assess the quality of cell populations identified in the initial analysis, where each cluster in **Figure S1F** was compared to the rest. Clusters that did not express a unique signature or those that express markers known to be mutually exclusive were removed; (2) To identify novel subclass markers (**Figure 2B**, **Figure S2D-E**). This was accomplished by comparing each subclass against the rest; (3) To identify type-specific markers within each subclass (**Figure S3A-C**). Here, each type was compared to other types of the same subclass; and (4) To identify gene expression changes as a result of visual deprivation. We performed DE between NR and DR (both ways) subclasses (**Figure 6A**, **Figure S6A**).

Identification of genes showing graded expression among L2/3 types

We compared each L2/3 type to the other two (e.g., A vs B and C) to identify 287 type-specific genes at fold change > 2 and p-value < 10^{-10} (Wilcoxon test). The expression levels of these genes were z-scored, and we used *k*-means clustering to identify *k*=7 groups based on their pattern of expression among the three types (**Figure S6A**). The optimal number of groups was identified using the elbow method. Five of the seven groups, containing 217 genes, showed graded expression differences that could be classified into one of the following patterns based on visual inspection: A > B > C (77 genes), A < B > C (36 genes), C > A > B (9 genes), C > B > A (85 genes) and A > C > B (10 genes). The remaining X genes were expressed in a digital fashion that fell into one of two groups: C > B = A (35 genes) and A > B = C (35 genes). Thus, approximately 75% of the DE genes among L2/3 types are expressed in a graded fashion.

Pseudo-spatial inference of gene expression in L2/3

FISH experiments targeting the three L2/3 glutamatergic type markers revealed that type A resides at the top (near the pia), type B in the middle, and type C at the bottom of L2/3, bordering L4 (**Figure 3**). Surprisingly, this relative positioning of A, B, and C types was mirrored in the UMAP embedding. We therefore hypothesized that the UMAP coordinates of a neuron may serve as a proxy for the approximate relative position of its soma in the tissue and used this to calculate the expected spatial expression profiles of genes in each dataset.

In each scenario, we marked the "A" and "C" cells furthest from each other on the UMAP space as the "root" and the "leaf" and assumed that these represent the top and bottom of L2/3 respectively. We used diffusion pseudo-time (DPT) [70,71] to order all L2/3 cells relative to the root cell. DPT and similar methods have been used previously to order cells based on their developmental state (i.e., pseudo-time); we have used it in this context to infer "pseudo-spatial" position based on the observed correspondence described above. Pseudo-spatial positions for cells were close to 0 at the top, where type A begins, and gradually increased through types B and C, reaching the maximum normalized value of 1 at the end of L2/3 in UMAP space. We performed this pseudo-spatial analysis for L2/3 neurons in each of the six normally reared samples.

For the DR and DL datasets, where the spatial organization and transcriptomic profiles are disrupted, a root cell was randomly selected from the beginning of L2/3 in UMAP space (e.g., a cell from the edge of cluster "L2/3_1" was chosen for P28DR) (**Figure 4B**). Finally, to visualize the expression of gradient genes as a function of pseudo-spatial position (**Figure 6F, H**), we averaged the expressions along bins of pseudo-spatial location that contained as many cells as ~10% of a given dataset.

Separation of cell classes and subclasses using Seurat

In addition to clustering each time separately in SCANPY, Seurat (version 3.1, [31] was used to cluster data from all times and conditions together. This analysis was done to evaluate class and subclass level clustering, and to provide a framework to broadly check

gene expression for FISH experiments in all subclasses at all times collectively. Seurat clustering was performed using two methods within Seurat with similar final results. In the log-normalization based method, data were log normalized and scaled to 10,000 transcripts per cell, with 2000 variable genes used. In the generalized linear model method "SCTransform" [72], normalization was used with 3000 variable genes. In both methods cells with fewer than 1000 or over 6000 genes or >1% mitochondrial content were filtered out. PCA was performed and unsupervised clustering was applied to the top 80 PCs. Major cell type markers from [1] and [20] were used to assign class and subclass designations to clusters. Clusters having two or more major markers were discarded as "doublet/debris" clusters, and clusters that were solely composed of one or two replicates were also discarded as debris clusters. In both log-normalization and SCT clustering by Seurat, the P8 cortico-cortical projecting excitatory neurons clustered separately from similar subclass neurons of later time points. Thus, P8 was clustered separately, and cell IDs from P8-only clustering were used to re-label the corresponding P8 cells in the full dataset. Class and subclass level clustering results matched SCANPY-based results (**Figure S2J**).

Differential gene expression analysis using Seurat

The Seurat-based clustering results were primarily used to assess subclass-level differentially expressed genes. Gene signatures of each cell subclass at different time points were identified with the `FindMarkers` function, performing pairwise time or condition comparisons and by comparing one time point to the average of others (a second method only used normally reared datasets). Genes were considered if they were present in 10% of cells, 0.25 log fold enriched (1.28 fold-change or more), and had a Benjamini-Hochberg corrected $P<0.05$. Of these, genes that were 0.4 log fold enriched (1.5-fold change or more) were classified as enriched.

Materials availability

Computational scripts detailing snRNA-seq analysis reported in this paper along with the raw expression matrices and processed h5ad files are available at https://github.com/shekharlab/mouseVC. All raw and processed snRNA-seq datasets

reported in this study will be made publicly available via NCBI's Gene Expression Omnibus (GEO). All data and custom software for imaging analysis will be made available upon request.

REFERENCES

1 Tasic, B. *et al.* Adult mouse cortical cell taxonomy revealed by single cell transcriptomics. *Nat Neurosci* **19**, 335-346, doi:10.1038/nn.4216 (2016).

2 Motta, A. *et al.* Dense connectomic reconstruction in layer 4 of the somatosensory cortex. *Science* **366**, doi:10.1126/science.aay3134 (2019).

3 Ackman, J. B., Burbridge, T. J. & Crair, M. C. Retinal waves coordinate patterned activity throughout the developing visual system. *Nature* **490**, 219-225, doi:10.1038/nature11529 (2012).

4 Katz, L. C. & Shatz, C. J. Synaptic activity and the construction of cortical circuits. *Science* **274**, 1133-1138, doi:10.1126/science.274.5290.1133 (1996).

5 Ko, H. *et al.* The emergence of functional microcircuits in visual cortex. *Nature* **496**, 96-100, doi:10.1038/nature12015 (2013).

6 Sanes, J. R. & Zipursky, S. L. Synaptic Specificity, Recognition Molecules, and Assembly of Neural Circuits. *Cell* **181**, 536-556, doi:10.1016/j.cell.2020.04.008 (2020).

7 Meister, M., Wong, R. O., Baylor, D. A. & Shatz, C. J. Synchronous bursts of action potentials in ganglion cells of the developing mammalian retina. *Science* **252**, 939-943, doi:10.1126/science.2035024 (1991).

8 Xu, H. P. *et al.* An instructive role for patterned spontaneous retinal activity in mouse visual map development. *Neuron* **70**, 1115-1127, doi:10.1016/j.neuron.2011.04.028 (2011).

9 Hooks, B. M. & Chen, C. Circuitry Underlying Experience-Dependent Plasticity in the Mouse Visual System. *Neuron* **107**, 986-987, doi:10.1016/j.neuron.2020.08.004 (2020).

10 Wiesel, T. N. & Hubel, D. H. Single-Cell Responses in Striate Cortex of Kittens Deprived of Vision in One Eye. *J Neurophysiol* **26**, 1003-1017, doi:10.1152/jn.1963.26.6.1003 (1963).

11 Hensch, T. K. Critical period plasticity in local cortical circuits. *Nat Rev Neurosci* **6**, 877-888, doi:10.1038/nrn1787 (2005).

12 Hensch, T. K. Critical period regulation. *Annu Rev Neurosci* **27**, 549-579, doi:10.1146/annurev.neuro.27.070203.144327 (2004).

13 Gordon, J. A. & Stryker, M. P. Experience-dependent plasticity of binocular responses in the primary visual cortex of the mouse. *J Neurosci* **16**, 3274-3286 (1996).

14 Tan, L., Tring, E., Ringach, D. L., Zipursky, S. L. & Trachtenberg, J. T. Vision Changes the Cellular Composition of Binocular Circuitry during the Critical Period. *Neuron* **108**, 735-747 e736, doi:10.1016/j.neuron.2020.09.022 (2020).

15 Espinosa, J. S. & Stryker, M. P. Development and plasticity of the primary visual cortex. *Neuron* **75**, 230-249, doi:10.1016/j.neuron.2012.06.009 (2012).

16 Wang, B. S., Sarnaik, R. & Cang, J. Critical period plasticity matches binocular orientation preference in the visual cortex. *Neuron* **65**, 246-256, doi:10.1016/j.neuron.2010.01.002 (2010).

17 Ko, H., Mrsic-Flogel, T. D. & Hofer, S. B. Emergence of feature-specific connectivity in cortical microcircuits in the absence of visual experience. *J Neurosci* **34**, 9812-9816, doi:10.1523/JNEUROSCI.0875-14.2014 (2014).

18 Jenks, K. R. & Shepherd, J. D. Experience-Dependent Development and Maintenance of Binocular Neurons in the Mouse Visual Cortex. *Cell Rep* **30**, 1982-1994 e1984, doi:10.1016/j.celrep.2020.01.031 (2020).
19 Tan, L., Ringach, D. L., Zipursky, S. L. & Trachtenberg, J. T. Vision is required for the formation of binocular neurons prior to the classical critical period. *BioRxiv*, doi:10.1101/2021.06.15.448591 (2021).
20 Tasic, B. *et al.* Shared and distinct transcriptomic cell types across neocortical areas. *Nature* **563**, 72-78, doi:10.1038/s41586-018-0654-5 (2018).
21 Hrvatin, S. *et al.* Single-cell analysis of experience-dependent transcriptomic states in the mouse visual cortex. *Nat Neurosci* **21**, 120-129, doi:10.1038/s41593-017-0029-5 (2018).
22 Majdan, M. & Shatz, C. J. Effects of visual experience on activity-dependent gene regulation in cortex. *Nat Neurosci* **9**, 650-659, doi:10.1038/nn1674 (2006).
23 Tropea, D. *et al.* Gene expression changes and molecular pathways mediating activity-dependent plasticity in visual cortex. *Nat Neurosci* **9**, 660-668, doi:10.1038/nn1689 (2006).
24 Favuzzi, E. *et al.* Distinct molecular programs regulate synapse specificity in cortical inhibitory circuits. *Science* **363**, 413-417, doi:10.1126/science.aau8977 (2019).
25 Hinojosa, A. J., Deogracias, R. & Rico, B. The Microtubule Regulator NEK7 Coordinates the Wiring of Cortical Parvalbumin Interneurons. *Cell Rep* **24**, 1231-1242, doi:10.1016/j.celrep.2018.06.115 (2018).
26 Li, M. *et al.* Synaptogenesis in the developing mouse visual cortex. *Brain Res Bull* **81**, 107-113, doi:10.1016/j.brainresbull.2009.08.028 (2010).
27 Wolock, S. L., Lopez, R. & Klein, A. M. Scrublet: Computational Identification of Cell Doublets in Single-Cell Transcriptomic Data. *Cell Syst* **8**, 281-291 e289, doi:10.1016/j.cels.2018.11.005 (2019).
28 Zeng, H. & Sanes, J. R. Neuronal cell-type classification: challenges, opportunities and the path forward. *Nat Rev Neurosci* **18**, 530-546, doi:10.1038/nrn.2017.85 (2017).
29 Yuste, R. *et al.* A community-based transcriptomics classification and nomenclature of neocortical cell types. *Nat Neurosci* **23**, 1456-1468, doi:10.1038/s41593-020-0685-8 (2020).
30 Yao, Z. *et al.* An integrated transcriptomic and epigenomic atlas of mouse primary motor cortex cell types. *BioRxiv*, doi:https://doi.org/10.1101/2020.02.29.970558 (2020).
31 Satija, R., Farrell, J. A., Gennert, D., Schier, A. F. & Regev, A. Spatial reconstruction of single-cell gene expression data. *Nat Biotechnol* **33**, 495-502, doi:10.1038/nbt.3192 (2015).
32 Kim, M. H., Znamenskiy, P., Iacaruso, M. F. & Mrsic-Flogel, T. D. Segregated Subnetworks of Intracortical Projection Neurons in Primary Visual Cortex. *Neuron* **100**, 1313-1321 e1316, doi:10.1016/j.neuron.2018.10.023 (2018).
33 Kim, E. J. *et al.* Extraction of Distinct Neuronal Cell Types from within a Genetically Continuous Population. *Neuron* **107**, 274-282 e276, doi:10.1016/j.neuron.2020.04.018 (2020).

34 Sudhof, T. C. The cell biology of synapse formation. *J Cell Biol* **220**, doi:10.1083/jcb.202103052 (2021).
35 Woo, J. *et al.* The adhesion protein IgSF9b is coupled to neuroligin 2 via S-SCAM to promote inhibitory synapse development. *J Cell Biol* **201**, 929-944, doi:10.1083/jcb.201209132 (2013).
36 Lu, W., Bromley-Coolidge, S. & Li, J. Regulation of GABAergic synapse development by postsynaptic membrane proteins. *Brain Res Bull* **129**, 30-42, doi:10.1016/j.brainresbull.2016.07.004 (2017).
37 Gangwar, S. P. *et al.* Molecular Mechanism of MDGA1: Regulation of Neuroligin 2:Neurexin Trans-synaptic Bridges. *Neuron* **94**, 1132-1141 e1134, doi:10.1016/j.neuron.2017.06.009 (2017).
38 Kim, J. A. *et al.* Structural Insights into Modulation of Neurexin-Neuroligin Trans-synaptic Adhesion by MDGA1/Neuroligin-2 Complex. *Neuron* **94**, 1121-1131 e1126, doi:10.1016/j.neuron.2017.05.034 (2017).
39 Cembrowski, M. S. *et al.* Spatial Gene-Expression Gradients Underlie Prominent Heterogeneity of CA1 Pyramidal Neurons. *Neuron* **89**, 351-368, doi:10.1016/j.neuron.2015.12.013 (2016).
40 Cembrowski, M. S. & Menon, V. Continuous Variation within Cell Types of the Nervous System. *Trends Neurosci* **41**, 337-348, doi:10.1016/j.tins.2018.02.010 (2018).
41 O'Leary, T. P. *et al.* Extensive and spatially variable within-cell-type heterogeneity across the basolateral amygdala. *Elife* **9**, doi:10.7554/eLife.59003 (2020).
42 Yao, Z. *et al.* A taxonomy of transcriptomic cell types across the isocortex and hippocampal formation. *Cell*, doi:10.1016/j.cell.2021.04.021 (2021).
43 Kurmangaliyev, Y. Z., Yoo, J., Valdes-Aleman, J., Sanfilippo, P. & Zipursky, S. L. Transcriptional Programs of Circuit Assembly in the Drosophila Visual System. *Neuron* **108**, 1045-1057 e1046, doi:10.1016/j.neuron.2020.10.006 (2020).
44 Ozel, M. N. *et al.* Neuronal diversity and convergence in a visual system developmental atlas. *Nature* **589**, 88-95, doi:10.1038/s41586-020-2879-3 (2021).
45 Shekhar, K. & Sanes, J. R. Generating and Using Transcriptomically Based Retinal Cell Atlases. *Annu Rev Vis Sci*, doi:10.1146/annurev-vision-032621-075200 (2021).
46 Han, Y. *et al.* The logic of single-cell projections from visual cortex. *Nature* **556**, 51-56, doi:10.1038/nature26159 (2018).
47 Harris, K. D. & Mrsic-Flogel, T. D. Cortical connectivity and sensory coding. *Nature* **503**, 51-58, doi:10.1038/nature12654 (2013).
48 Greenberg, M. E., Ziff, E. B. & Greene, L. A. Stimulation of neuronal acetylcholine receptors induces rapid gene transcription. *Science* **234**, 80-83, doi:10.1126/science.3749894 (1986).
49 Gray, J. M. & Spiegel, I. Cell-type-specific programs for activity-regulated gene expression. *Curr Opin Neurobiol* **56**, 33-39, doi:10.1016/j.conb.2018.11.001 (2019).
50 Tyssowski, K. M. *et al.* Different Neuronal Activity Patterns Induce Different Gene Expression Programs. *Neuron* **98**, 530-546 e511, doi:10.1016/j.neuron.2018.04.001 (2018).

51 Nakashima, A. *et al.* Structured spike series specify gene expression patterns for olfactory circuit formation. *Science* **365**, doi:10.1126/science.aaw5030 (2019).
52 Yap, E. L. & Greenberg, M. E. Activity-Regulated Transcription: Bridging the Gap between Neural Activity and Behavior. *Neuron* **100**, 330-348, doi:10.1016/j.neuron.2018.10.013 (2018).
53 Holtmaat, A. & Svoboda, K. Experience-dependent structural synaptic plasticity in the mammalian brain. *Nat Rev Neurosci* **10**, 647-658, doi:10.1038/nrn2699 (2009).
54 Morales, B., Choi, S. Y. & Kirkwood, A. Dark rearing alters the development of GABAergic transmission in visual cortex. *J Neurosci* **22**, 8084-8090 (2002).
55 Hensch, T. K. *et al.* Local GABA circuit control of experience-dependent plasticity in developing visual cortex. *Science* **282**, 1504-1508, doi:10.1126/science.282.5393.1504 (1998).
56 Trapnell, C. Defining cell types and states with single-cell genomics. *Genome Res* **25**, 1491-1498, doi:10.1101/gr.190595.115 (2015).
57 Shekhar, K. *et al.* Comprehensive Classification of Retinal Bipolar Neurons by Single-Cell Transcriptomics. *Cell* **166**, 1308-1323 e1330, doi:10.1016/j.cell.2016.07.054 (2016).
58 Tran, N. M. *et al.* Single-Cell Profiles of Retinal Ganglion Cells Differing in Resilience to Injury Reveal Neuroprotective Genes. *Neuron* **104**, 1039-1055 e1012, doi:10.1016/j.neuron.2019.11.006 (2019).
59 McInnes, L., Healy, J. & Melville, J. Umap: Uniform manifold approximation and projection for dimension reduction. *arXiv preprint* **1802.03426** (2018).
60 Franklin, K. P., G. *Paxinos and Franklin's the Mouse Brain in Stereotaxic Coordinates, Compact*. 4th edn, (Elsevir, 2012).
61 Kishi, J. Y. *et al.* SABER amplifies FISH: enhanced multiplexed imaging of RNA and DNA in cells and tissues. *Nat Methods* **16**, 533-544, doi:10.1038/s41592-019-0404-0 (2019).
62 McQuin, C. *et al.* CellProfiler 3.0: Next-generation image processing for biology. *PLoS Biol* **16**, e2005970, doi:10.1371/journal.pbio.2005970 (2018).
63 Arneson, D. *et al.* Single cell molecular alterations reveal target cells and pathways of concussive brain injury. *Nat Commun* **9**, 3894, doi:10.1038/s41467-018-06222-0 (2018).
64 Wolf, F. A., Angerer, P. & Theis, F. J. SCANPY: large-scale single-cell gene expression data analysis. *Genome Biol* **19**, 15, doi:10.1186/s13059-017-1382-0 (2018).
65 Peng, Y. R. *et al.* Molecular Classification and Comparative Taxonomics of Foveal and Peripheral Cells in Primate Retina. *Cell* **176**, 1222-1237 e1222, doi:10.1016/j.cell.2019.01.004 (2019).
66 Traag, V. A., Waltman, L. & van Eck, N. J. From Louvain to Leiden: guaranteeing well-connected communities. *Sci Rep* **9**, 5233, doi:10.1038/s41598-019-41695-z (2019).
67 Becht, E. *et al.* Dimensionality reduction for visualizing single-cell data using UMAP. *Nat Biotechnol*, doi:10.1038/nbt.4314 (2018).

68 Korsunsky, I. *et al.* Fast, sensitive and accurate integration of single-cell data with Harmony. *Nat Methods* **16**, 1289-1296, doi:10.1038/s41592-019-0619-0 (2019).

69 Chen, T. & Guestrin, C. XGBoost: A Scalable Tree Boosting System. *arXiv* **1603.02754v3**, doi:10.1145/2939672.2939785 (2016).

70 Haghverdi, L., Buettner, F. & Theis, F. J. Diffusion maps for high-dimensional single-cell analysis of differentiation data. *Bioinformatics* **31**, 2989-2998, doi:10.1093/bioinformatics/btv325 (2015).

71 Wolf, F. A. *et al.* PAGA: graph abstraction reconciles clustering with trajectory inference through a topology preserving map of single cells. *Genome Biol* **20**, 59, doi:10.1186/s13059-019-1663-x (2019).

72 Hafemeister, C. & Satija, R. Normalization and variance stabilization of single-cell RNA-seq data using regularized negative binomial regression. *Genome Biol* **20**, 296, doi:10.1186/s13059-019-1874-1 (2019).

FIGURES, TITLES, AND LEGENDS

Figure 1

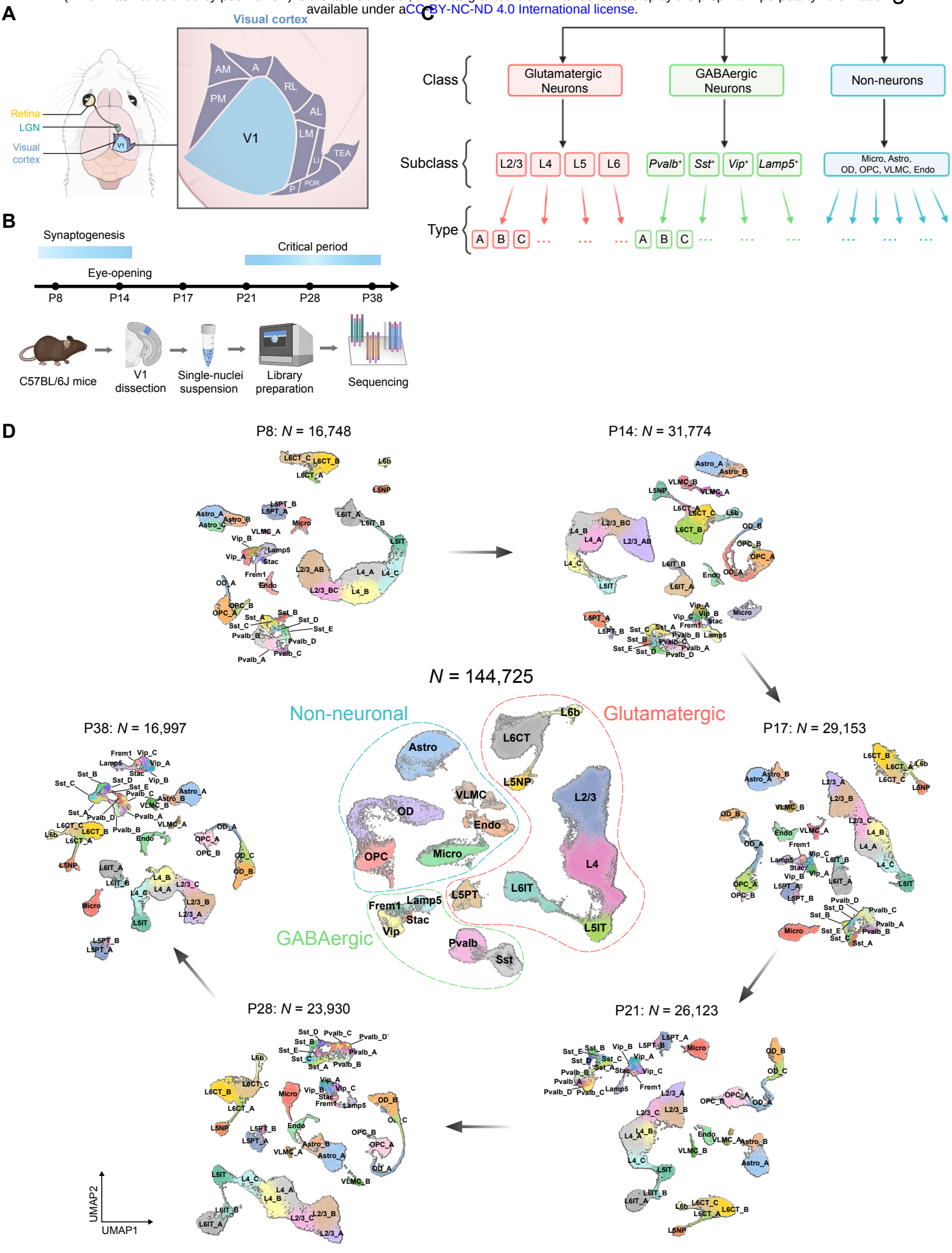

Figure 1. snRNA-seq profiling of V1 during postnatal development

A. Schematic of the mouse visual system. Visual information predominantly passes from the retina to the contralateral visual cortex through the lateral geniculate nucleus (LGN). Some visual information from the ipsilateral eye also passes through the LGN to the ipsilateral cortex (not shown). Inset shows a magnified view of the primary visual cortex (V1) and surrounding higher visual areas. Abbreviations: A, anterior; AL, anterolateral; AM, anteromedial; LI, laterointermediate; LM, lateromedial; P, posterior; PM, posteromedial; POR, postrhinal; RL, rostrolateral; TEA, temporal anterior areas.

B. Experimental workflow of snRNA-seq profiling of V1 at six postnatal ages (see **Methods** for details).

C. Cellular taxonomy of V1 showing the hierarchical organization of transcriptomic classes, subclasses, and types.

D. Uniform Manifold Approximation and Projection (UMAP) visualization of V1 transcriptomic diversity during postnatal development [59]. Dots correspond to cells and distances between them reflect degrees of transcriptomic similarity. Central panel shows cells from all six ages colored by subclass identity (**Table S1**). The six peripheral panels show cells from different ages, colored by type identity determined via clustering. Data from each age and class were analyzed separately and then merged together for visualization purposes (**Methods**).

Figure 2

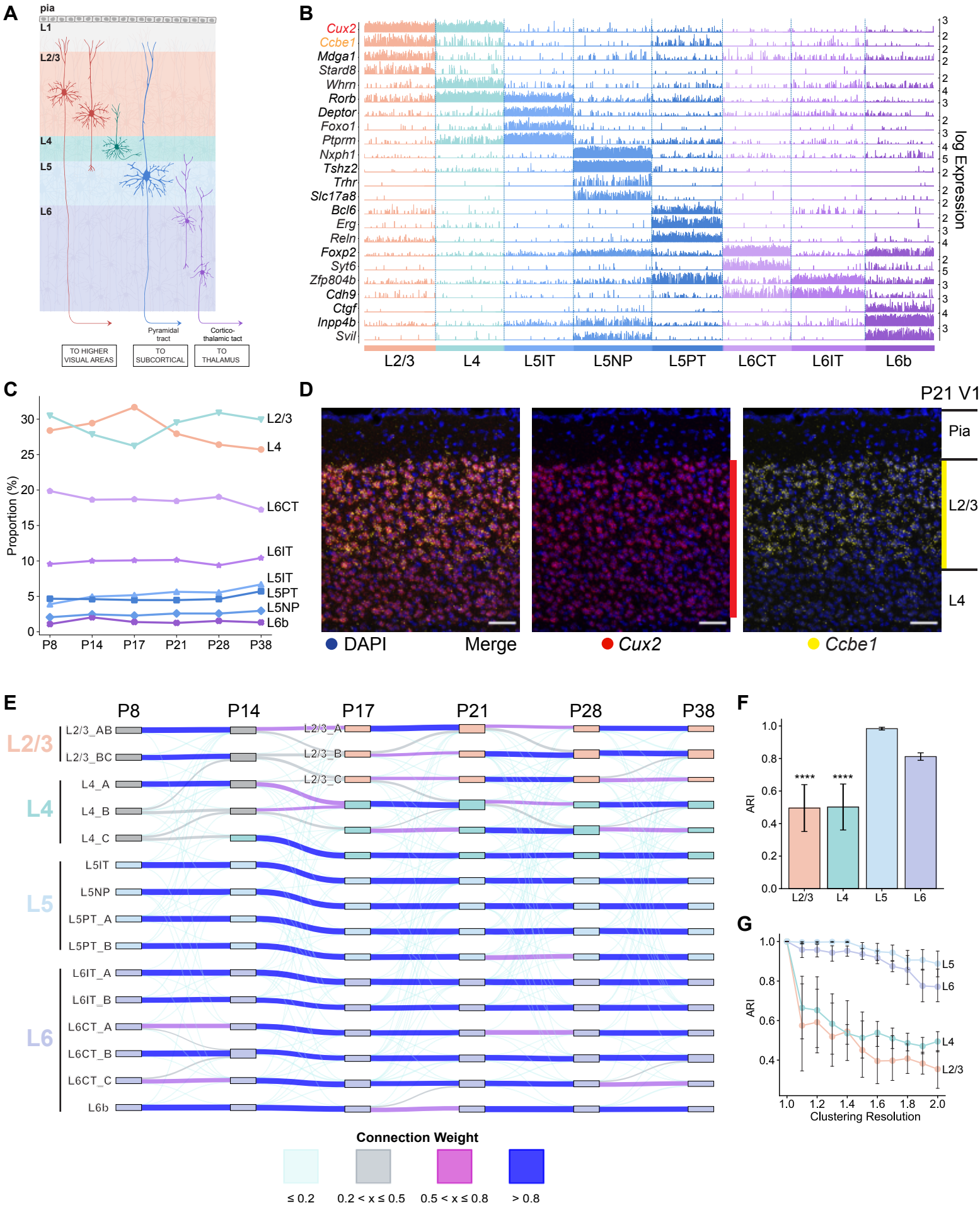

Figure 2. Transcriptomic diversity of V1 glutamatergic neurons during postnatal development

A. Schematic of glutamatergic neurons in V1 arranged in layers L1-L6.

B. Tracks plot showing subclass-specific markers (rows) in glutamatergic neurons (columns), grouped by subclass (annotation bar, bottom). 1000 randomly selected cells from each subclass were used for plotting. For each gene, the scale on the y-axis (right) corresponds to normalized, log-transformed transcript counts detected in each cell. *Ccbe1*, a L2/3 marker, and *Cux2*, a L2/3/4 marker, are highlighted.

C. Line plots showing that the proportions of glutamatergic subclasses are stable with age despite significant variation in the number of cells profiled (**Table S2**).

D. *Ccbe1* is a selective marker for L2/3 glutamatergic neurons. By contrast, *Cux2*, which is expressed in L2/3 and L4 glutamatergic neurons, is also expressed in inhibitory neurons and non-neuronal cells (also see **Figure S2B**). Panels show a coronal section through V1 analyzed by fluorescent *in situ* hybridization (FISH) at P21 (see **Figure S2** for other ages).

E. Transcriptomic similarity is used to identify temporal associations among V1 glutamatergic neuron types across ages. Shown is a Sankey diagram, where nodes denote individual V1 glutamatergic neuron types at each age (as in **Figure 1D**), and edges are colored based on transcriptomic correspondence, determined using a supervised classification approach (see **Methods** for explanation). Darker colors indicate higher correspondence.

F. Adjusted Rand Index (ARI) values quantifying temporal correspondence of glutamatergic types between each pair of consecutive ages based on transcriptomic similarity. Individual bars denote layers. ARI ranges from 0 (no correspondence) to 1 (perfect correspondence). Bar heights, mean ARI computed across pairs of consecutive ages; error bars, standard deviation; ***, $P<0.0001$ (one-way ANOVA) for layers 2/3 and 4 against layers 5 and 6.

G. Types in L2/3 and L4, but not L5 and L6, are sensitive to changes in clustering resolution. Glutamatergic neurons at each age are re-clustered at different values of the resolution parameter (x-axis), and the results are compared with the base

case corresponding to resolution = 1 (**Methods**). Line plots show mean ARI values for each layer (colors), while error bars denote standard deviation across different ages.

Figure 3

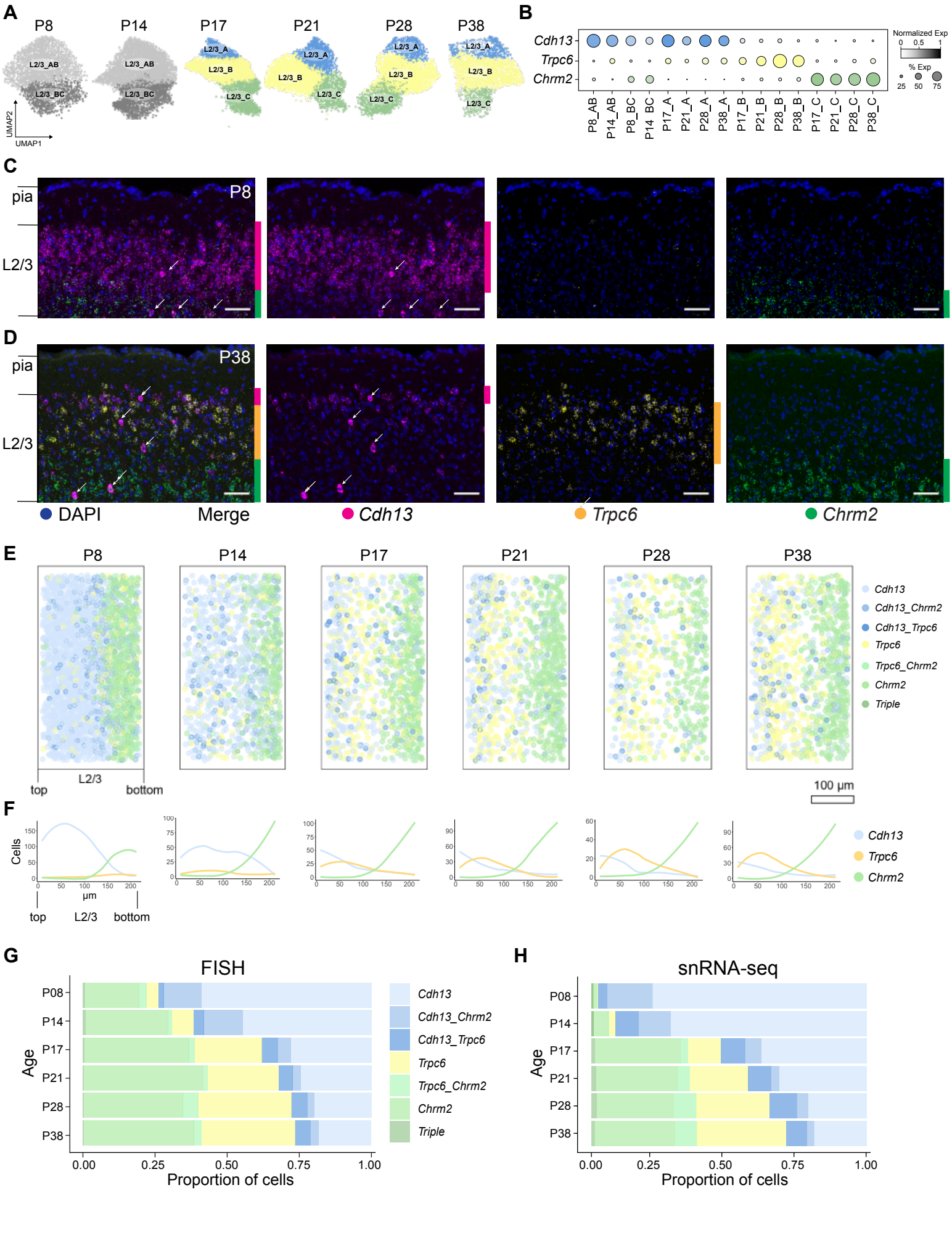

Figure 3. Anatomical and transcriptomic maturation of L2/3 glutamatergic neuron types

A. UMAP visualization of L2/3 glutamatergic neuron types across ages.
B. Dot plot showing expression patterns of L2/3 type-specific genes (rows and colors) across L2/3 neuron types arranged by age (columns). Dot size represents the proportion of cells with non-zero transcript counts, and shading depicts log-transformed expression levels.
C. FISH images showing type markers *Cdh13, Trpc6,* and *Chrm2* within L2/3 at P8. Vertical bars on the right of each image indicate sublayers expressing the indicated markers. Arrows, inhibitory neurons expressing *Cdh13*. Scale bar, 50 μm.
D. Same as C, at P38. Arrows, inhibitory neurons expressing *Cdh13*. Scale bar, 50 μm.
E. Pseudo-colored representation of *Cdh13, Trpc6,* and *Chrm2* expression in L2/3 cells across the six ages. Cells are grouped based on their expression levels of one or more of these markers (see legend on the right; **Methods**). Each panel is an overlay of five or six images of V1 from three mice. Pial to ventricular axis is oriented horizontally from left to right within each panel. Total number of cells analyzed: P8, 2324; P14, 1142; P17, 1036; P21, 1038; P28, 653; and P38, 1034. Scale bar, 100 μm.
F. Line tracings quantifying the number of cells per bin at each position along the pial to ventricular axis corresponding to panel E. 0 on the x-axis is the region of L2/3 closest to pia. 14 bins were used over the depth of L2/3.
G. Relative proportions of cells within each expression group defined in panel E quantified using FISH data.
H. Relative proportions of L2/3 cells within each expression group defined in panel E quantified using snRNA-seq data.

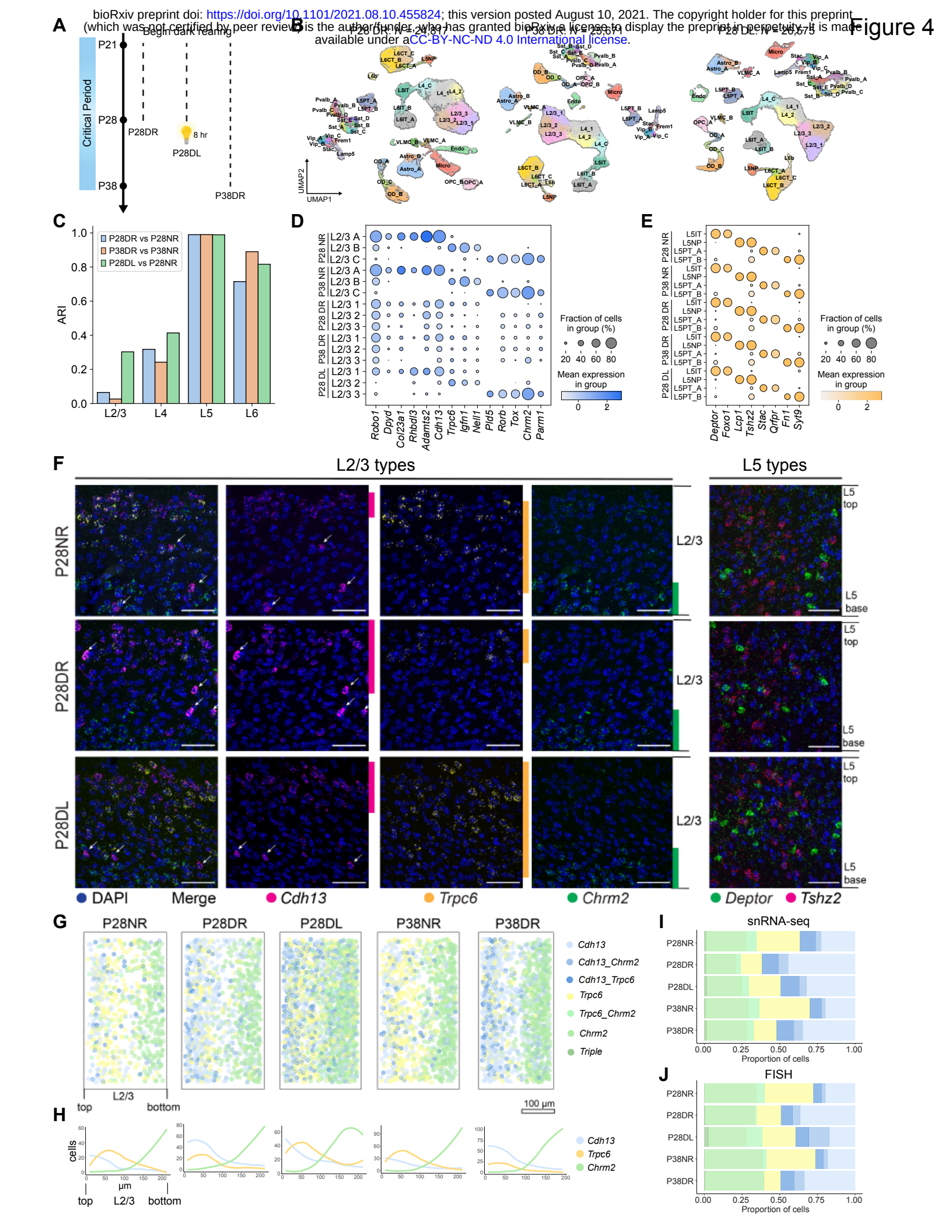

Figure 4. Visual experience is required to maintain L2/3 glutamatergic neuron types

A. Schematic of experiments to probe the influence of visual input on V1 transcriptomic identities. Data were collected from three rearing conditions: Dark-reared between P21-P28 and snRNA-seq profiling (P28DR), dark-reared between P21-P38 and snRNA-seq profiling (P38DR), and dark-reared between P21-P28 followed by 8h of ambient light stimulation and snRNA-seq profiling (P28DL).

B. UMAP visualization of transcriptomic diversity in P28DR (*left*), P38DR (*middle*), and P28DL (*right*). Clusters that match 1:1 to normally-reared (NR) types in **Figure 1D** are labeled accordingly. This was not possible for all L2/3 and two L4 clusters, which correspond poorly to NR types. We therefore provisionally labeled these clusters L2/3_1, L2/3_2, L2/3_3, L4_1, and L4_2.

C. Bar plot showing the Adjusted Rand Index (ARI) quantifying transcriptomic similarity within each layer (x-axis) between glutamatergic clusters observed in dark-reared mice and types observed in normally-reared (NR) mice. Colors correspond to comparisons: P28DR vs. P28NR, P38DR vs. P38NR, and P28DL vs. P28NR.

D. Expression of L2/3 type markers (columns) in NR, DR, and DL types and clusters (rows) at P28 and P38.

E. Same as panel D for L5. DR and DL clusters are labeled based on their tight transcriptomic correspondence with NR types (**Figure S5F, G**).

F. FISH images showing expression of L2/3 and L5 type markers in NR (*top row*), DR (*middle row*), and DL (*bottom row*) at P28. *Deptor* is a marker for L5IT and *Tshz2* is a marker for L5NP. Arrows, inhibitory neurons expressing *Cdh13*. Scale bar, 50 µm.

G. Pseudo-colored representation of *Cdh13, Trpc6,* and *Chrm2* expression in L2/3 cells in NR, DR, and DL mice at P28 and P38 (see legend on the right). Each plot is an overlay of 5-6 images of V1 from three mice. Pial to ventricular axis is oriented horizontally from left to right within each panel. Total number of cells analyzed: P28NR, 653; P28DR, 989; P28DL, 1732; P38NR, 1034; and P38DR, 1177). Scale bar, 100 µm.

H. Line tracings quantifying the number of cells per bin at each position along the pial to ventricular axis corresponding to panel G. 0 on the x-axis is the region of L2/3 closest to pia. 14 bins were used over the depth of L2/3.

I. Relative proportions of L2/3 cells within each expression group defined in panel G quantified using snRNA-seq data

J. Relative proportions of cells within each expression group defined in panel G quantified using FISH data.

Figure 5

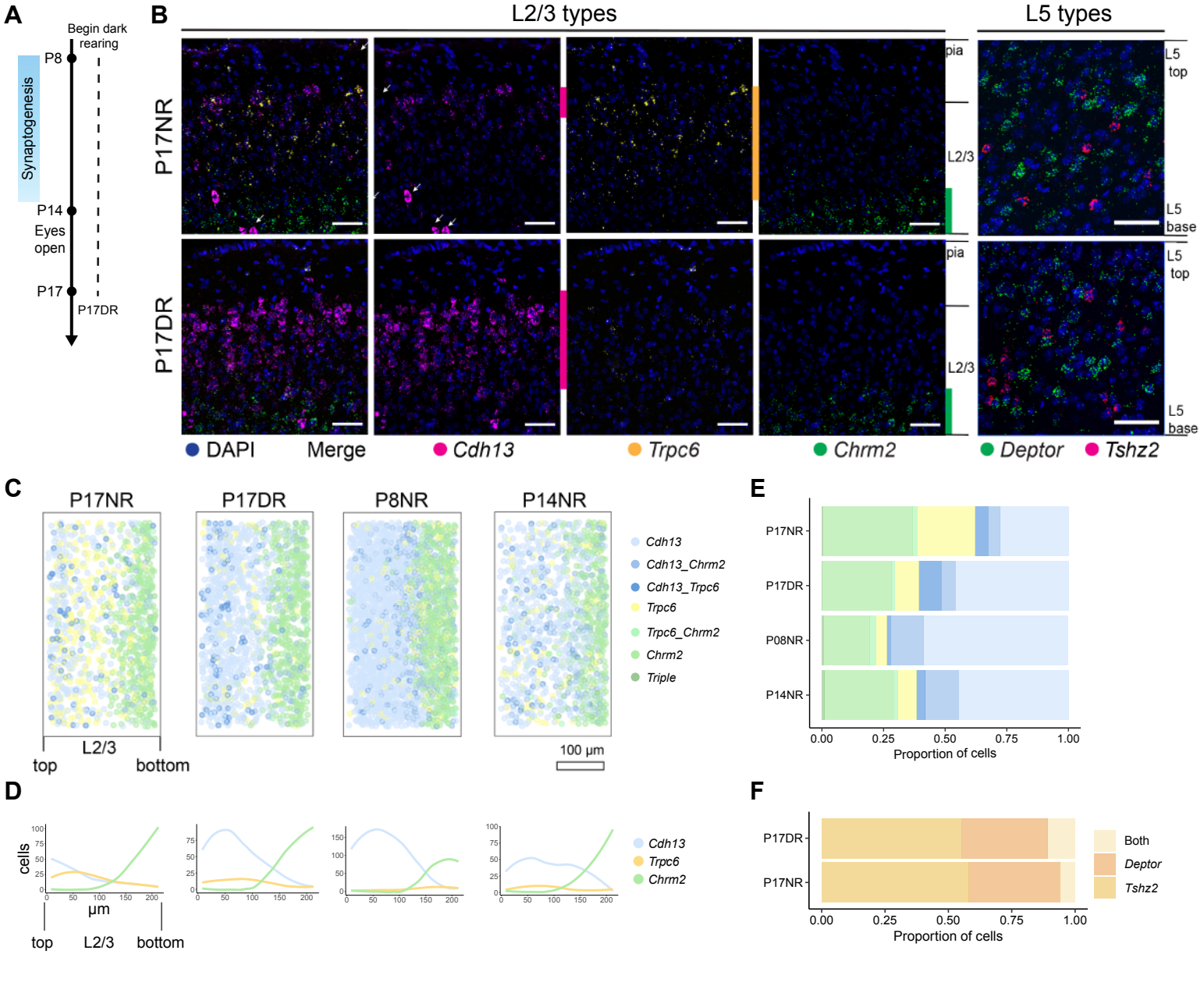

Figure 5. Vision is required to establish L2/3 glutamatergic neuron types

A. Schematic of experiments to probe the role of vision in establishing three L2/3 glutamatergic types.

B. FISH images showing expression of L2/3 and L5 type markers in normally-reared (NR) and dark reared (DR) mice at P17. Arrows, inhibitory neurons expressing *Cdh13*. Scale bar, 50 µm. *Deptor* is a marker for L5IT and *Tshz2* is a marker for L5NP.

C. Pseudo-colored representation of *Cdh13, Trpc6,* and *Chrm2* expression in L2/3 cells (see legend on the right). Each plot is an overlay of 6 images of V1 from three mice. Total number of cells analyzed: P17NR, 1036; P17DR, 1411.

D. Line tracings quantifying number of cells per bin at each position along the pial to ventricular axis corresponding to panel C. 0 on the x axis is the region of L2/3 closest to pia. 14 bins were used over the depth of L2/3.

E. Relative proportions of cells within each expression group defined in panel C quantified using FISH data.

F. Relative proportions of two L5 cell types, L5IT (*Deptor*$^{+}$) and L5NP (*Tshz2*$^{+}$) in normal and dark reared mice at P17. Total number of cells analyzed: P17NR, 1676; P17DR, 1544.

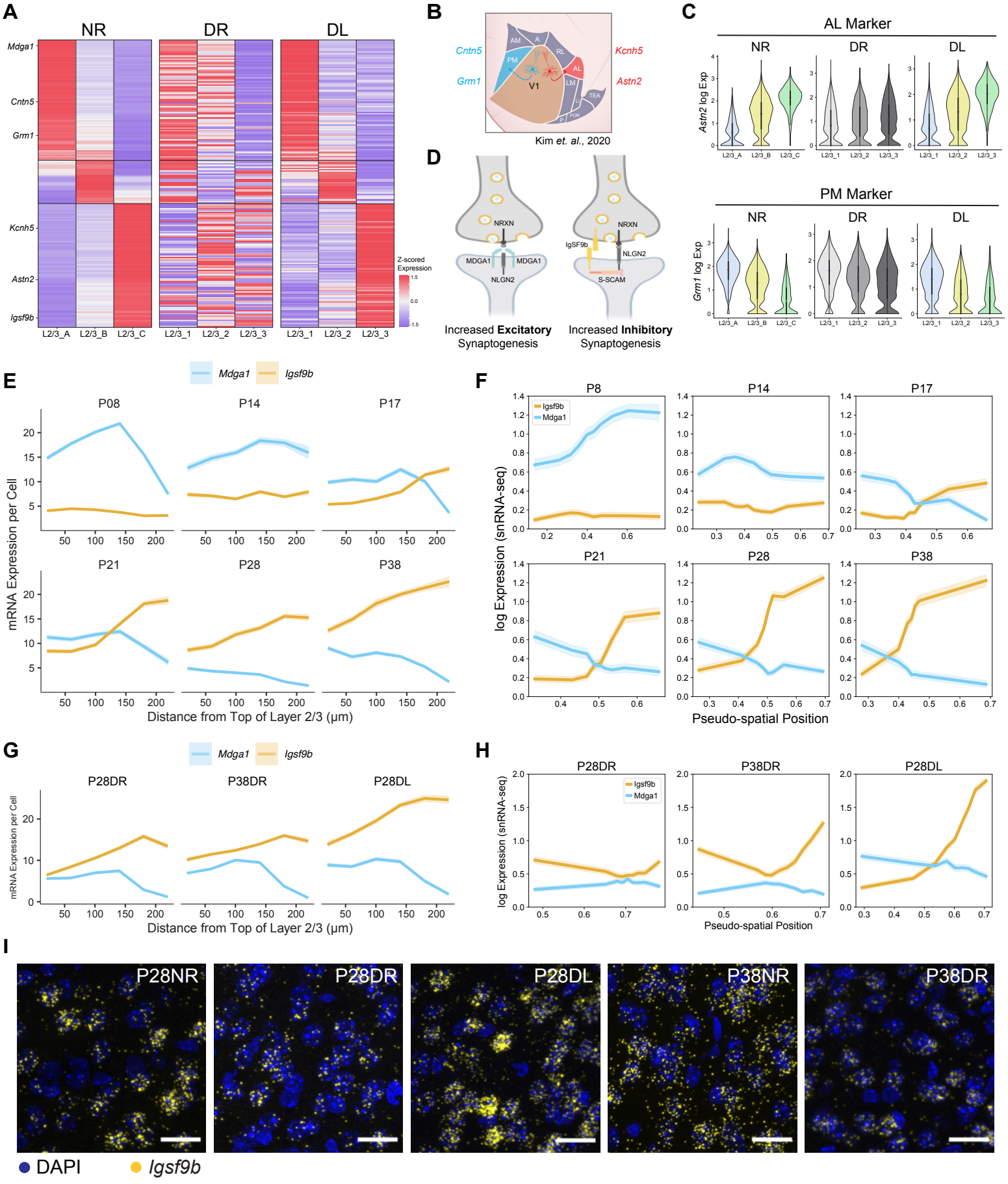

Figure 6. Continuous variation of L2/3 neuron types and vision-dependent gene gradients implicated in wiring

A. Heatmap of L2/3 type-specific genes showing graded expression in normally-reared mice (NR, *left panel*). This is disrupted in dark-reared mice (DR, *middle panel*) and partially recovered in dark-light adapted mice (DL, *right panel*). For the full set of L2/3 type-specific genes grouped by expression pattern, see **Figure S6A**.

B. Schematic highlighting the anterolateral (AL) and posteromedial (PM) higher visual areas. Genes preferentially expressed by L2/3 neurons projecting to AL or PM are indicated. Colors identified by retrograde labeling experiments are listed [33].

C. Violin plots comparing the expression levels of AL (top) and PM (bottom) markers listed in panel B in L2/3 cell types among NR, DR, and DL mice at P28.

D. Schematic of MDGA1 and IGSF9B interactions with NLGN2 at synapses. MDGA1 dimers prevent NLGN2 interaction with NRXN presynaptically. IGSF9B binds homophilically across the synapse and interacts with S-SCAM postsynaptically to stabilize NLGN2 interaction with NRXN.

E. FISH quantification of average *Mdga1* and *Igsf9b* expression (y-axis) in glutamatergic cells as a function of distance from the top of L2/3 (x-axis). Shaded ribbons represent standard error of the mean. Panels represent different ages. Cell numbers at each age: P8, 2204; P14, 928; P17, 1037; P21: 1183; P28, 719; and P38: 942 cells. Data collected from three to four animals at each age.

F. Reconstruction of *Mdga1* and *Igsf9b* expression levels averaged across cells based on their inferred L2/3 pseudo-spatial locations in UMAP space (see **Methods** for details). Shaded ribbons represent standard deviation.

G. Same as panel E for P28DR, P38DR, and P28DL. Cell numbers: P28DR, 1061; P38DR, 1383; and P28DL, 1053 cells. Data collected from three animals at each time point

H. Same as panel F for P28DR, P38DR, and P28DL.

I. Dark rearing decreases *Igsf9b* expression in L2/3, and brief ambient light exposure restores expression. Panels are labeled based on age and rearing condition. Scale bar, 50 μm.

SUPPLEMENTAL FIGURES, TITLES, AND LEGENDS

Figure S1

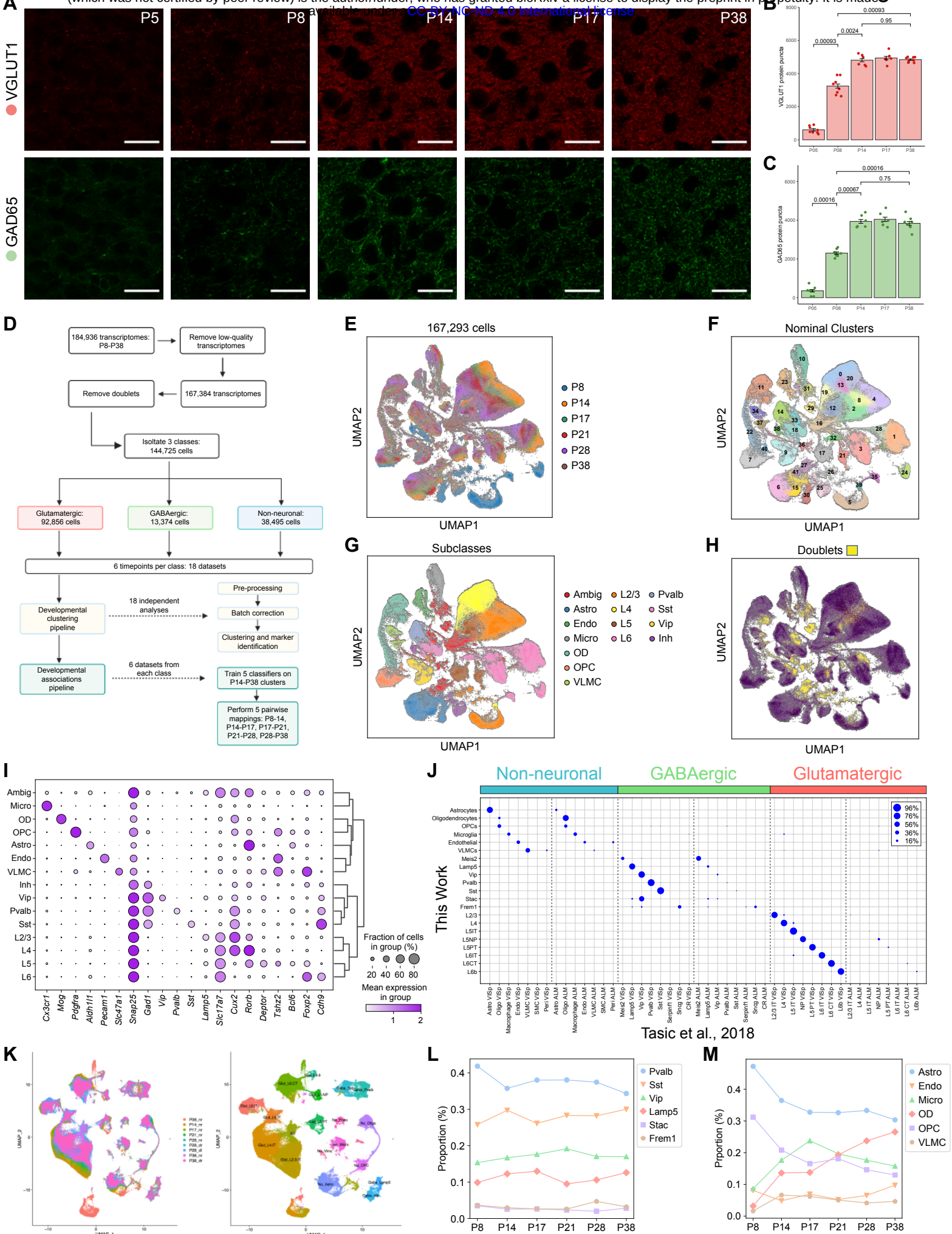

Figure S1. Expression of GABAergic and glutamatergic markers with age, snRNA-seq data pre-processing, and comparison to transcriptomic signatures of adult visual and motor cortices (Tasic *et al.,* 2018)

A. Immunohistochemical analysis of the expression of VGLUT1 (a glutamatergic marker) and GAD65 (a GABAergic marker) with age. Panels show single confocal images of VGLUT1 (red) and GAD65 (green) during postnatal development in L2/3 of V1 in wild-type mice. Ages are indicated on the top right corner panels in the top row. Scale bar, 20 μm.

B. VGLUT1 protein puncta quantification over time, n = 3-4 mice per age, quantified by slide imaged. Horizontal bars show p-values corresponding to a comparison of the number of puncta between each pair of ages using the Wilcoxon rank-sum test. Bar heights denote mean value, error bars are ± SEM.

C. Same as B, for GAD65 protein puncta.

D. A graphical summary of the computational pipeline used to define cell classes, subclasses, and types at each age in normally-reared (NR) mice and to analyze the maturation of types. A similar pipeline was used for analyzing the data obtained from dark-rearing (DR) and dark-light adaptation (DL) experiments described in **Figure 4**. See **Methods** for details.

E. Uniform Manifold Approximation (UMAP) visualization of V1 transcriptomes prior to removing doublets. Individual nuclei are colored by age.

F. Same as E, colored by transcriptomically defined clusters. This nominal clustering was used to identify and discard doublets and contaminants (**Methods**).

G. Same as E, with nuclei colored by their subclass identity. Clusters in F were assigned to subclasses based on known gene markers (**Table S1).**

H. Same as E, with computationally identified doublets highlighted in yellow. The doublets were identified using Scrublet, a nearest-neighbor classification framework that uses the data to simulate multiplets [27]. A post hoc analysis verified that the computationally identified doublets co-expressed markers from distinct classes and subclasses (**Table S1)** and were discarded prior to further analysis.

I. Dot plot showing marker genes (columns) that distinguish subclasses (rows) identified in panel G. The group labeled “Inh” is an admixture of inhibitory neuronal

subclasses defined by *Lamp5, Stac,* and *Frem1* that were not separated at this stage. The size of each dot represents the fraction of cells in each subclass with non-zero expression and its color denotes the average normalized expression level.

J. Confusion matrix showing transcriptomic correspondence between subclasses identified in this study (rows) and subclasses (columns) reported in a scRNA-seq survey of the adult primary visual cortex (V1) and the anterior lateral motor cortex (ALM) [20]. The size of each dot represents the proportion of each row mapped to an adult cortex subclass based on an XGBoost classifier trained on the adult cortex. Each row of the matrix is normalized to sum to 100%. The specific pattern of mapping indicates that the transcriptomic correspondence at the level of classes and subclasses was robust despite differences in RNA source (nuclei vs. cells), age (P8-P38 vs. P70+), and sequencing methods (e.g., droplet-based and plate-based). Glutamatergic and GABAergic subclasses map specifically to their V1 counterparts, reflecting regional specificity. Non-neuronal cells, on the other hand, mapped promiscuously, suggesting shared transcriptional programs between V1 and ALM for this class.

K. UMAP visualization of subclass separation when the same dataset is analyzed using Seurat (**Methods**). (*Left*) colored by sample ID, (*right*) colored by subclass. X_0 denotes low quality cells that were discarded.

L. Line plots showing that the relative proportions of GABAergic neuronal subclasses remain stable with age despite significant variation in the number of nuclei collected (**Table S2**).

M. Line plots showing relative proportions vs. age for non-neuronal subclasses.

Figure S2

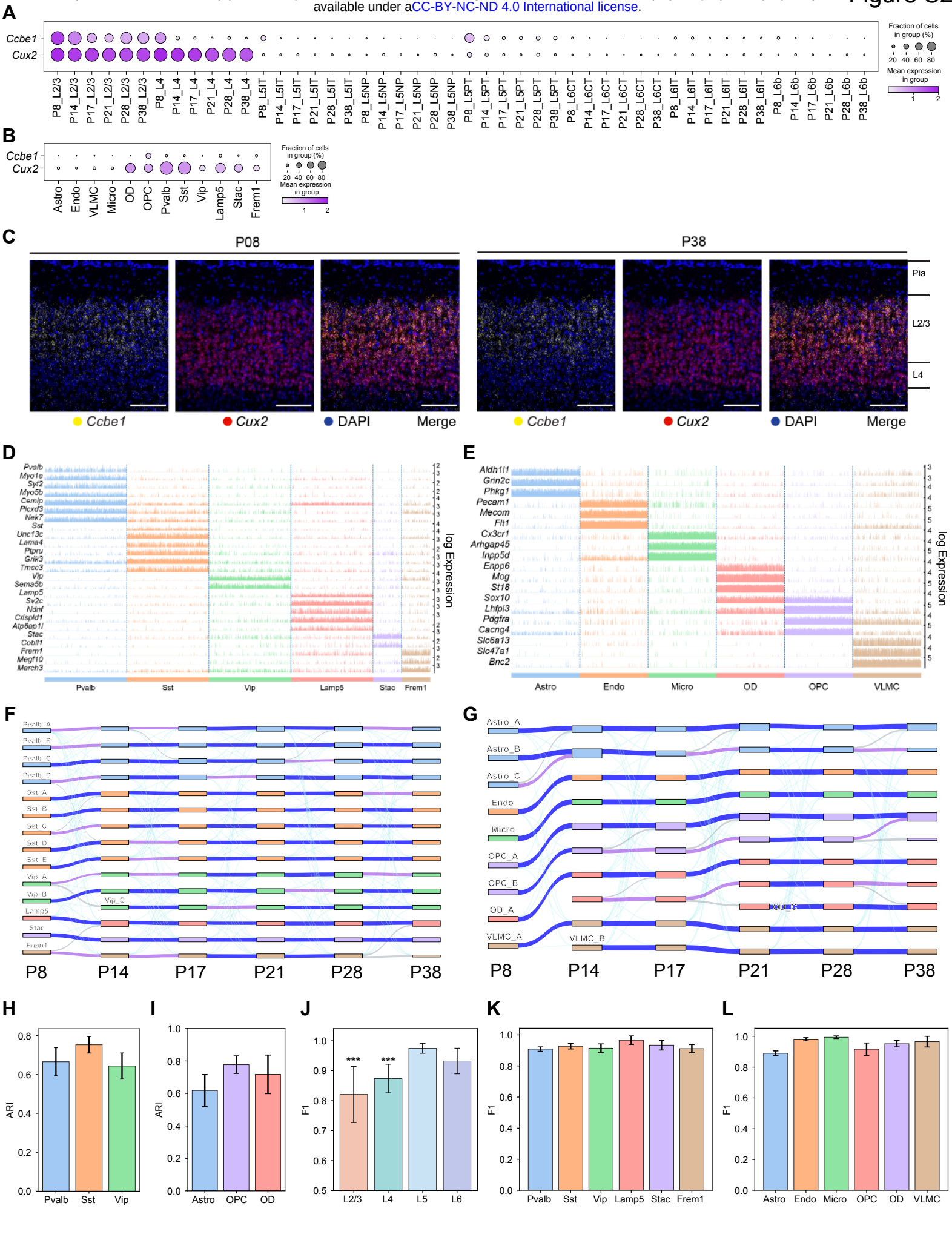

Figure S2. Additional data related to transcriptomic maturation of V1 cell types

A. *Ccbe1* is specific at all ages to L2/3 glutamatergic neurons (note transient expression in L5PT at P8), whereas *Cux2* is expressed in both L2/3 and L4 glutamatergic neurons throughout development.

B. *Cux2* is also expressed in GABAergic neurons and some non-neuronal subclasses, while *Ccbe1* is not. Thus, *Ccbe1* is a bona fide L2/3 glutamatergic neuron-specific marker.

C. FISH images from coronal sections show that *Cux2* is expressed in L2/3 and L4 while *Ccbe1* is selectively expressed in L2/3 glutamatergic neurons at P8 and P38. Scale bar, 100 µm.

D. Tracks plot showing subclass-specific markers (rows) in inhibitory neurons (columns). For each gene, the scale on the y-axis (right) corresponds to normalized, log-transformed transcript counts detected in each cell. Columns are grouped and colored based by subclass (annotation bar, bottom). In addition to the well-known subclasses marked by *Pvalb*, *Sst* and *Vip,* we also identify subclasses of GABAergic neurons marked by the selective expression of *Lamp5*, *Stac* and *Frem1*. These subclasses were collapsed together in the group labeled “Inh” in **Figure S1I**.

E. Same as panel D for non-neuronal subclasses.

F. Sankey graph showing the transcriptomic maturation of V1 GABAergic types. Representation as in **Figure 2E**.

G. Same as F for non-neuronal types.

H. Adjusted Rand Index (ARI) values quantifying temporal specificity during maturation of inhibitory types within each subclass. ARI is a measure of similarity between two ways of grouping the data, with values ranging from 0 (no correspondence) to 1 (perfect correspondence). For each subclass at each age, ARI values are computed by comparing the cluster identity of cells with the identity assigned by a multiclass classifier trained on the subsequent age. Individual bars denote the three inhibitory subclasses containing more than 2 types each. Subclasses *Lamp5*, *Stac* and *Frem1* are not shown as these could not be

satisfactorily subdivided into constituent types in this study. Bar heights, mean ARI computed across pairs of consecutive ages; error bars, standard deviation.

I. Same as panel H for non-neuronal subclasses. Subclasses Micro and Endo are not included as they each contain only one type.

J. F1 score values quantifying the degree of transcriptomic separation among types within each glutamatergic layer. Each bar represents the average F1 score calculated for types from each layer across all ages. $P^{***}<0.0001$ for comparison between L2/3 and L5/L6 and L4 and L5/6.

K. Same as panel J for GABAergic types.

L. Same as panel J for non-neuronal types.

Figure S3

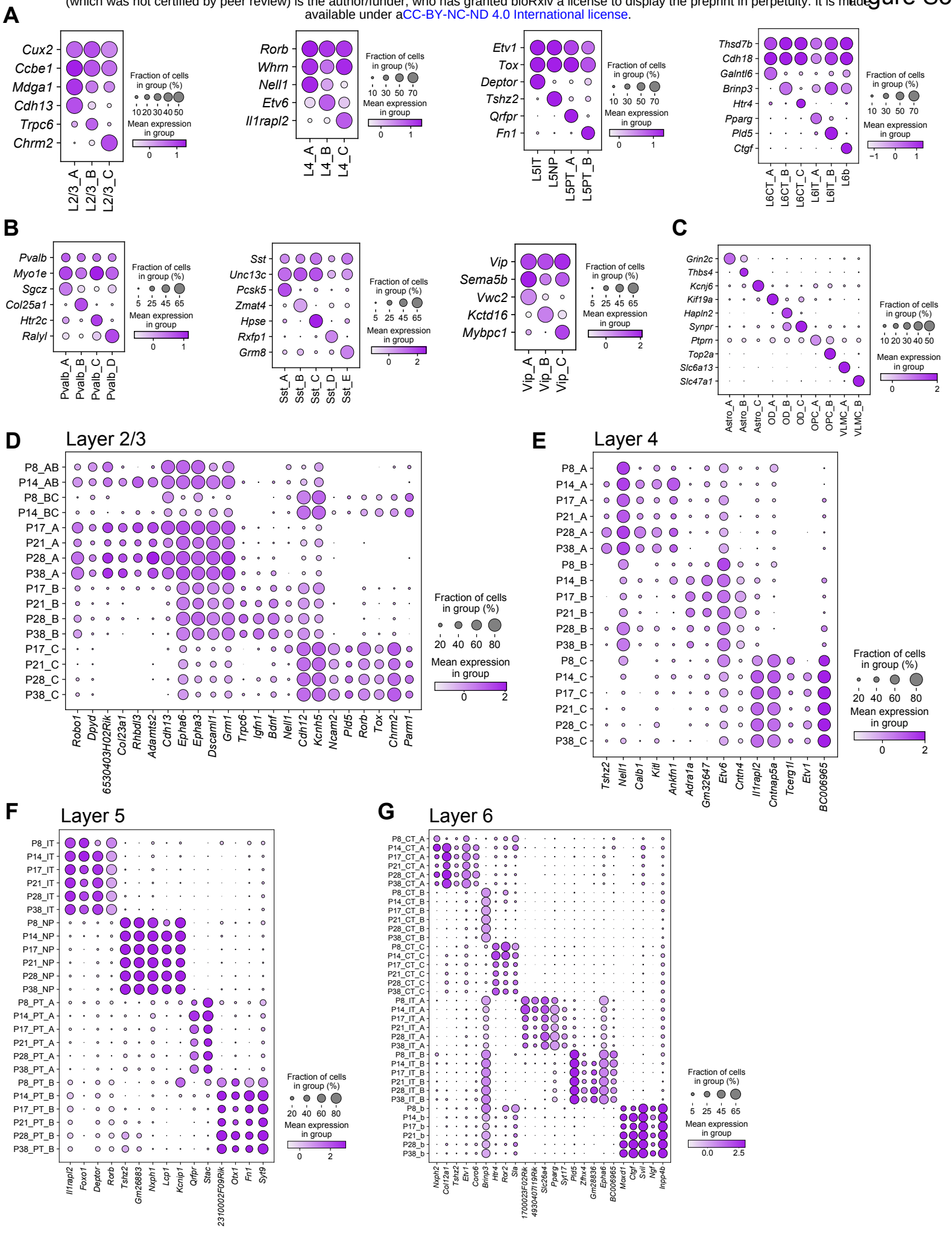

Figure S3. Cell type-specific markers for glutamatergic, GABAergic and non-neuronal subclasses

A. Dot plot showing markers (rows) for glutamatergic types (columns) within each subclass (panels, left to right). Within each subclass panel, the top two genes (rows) represent markers shared by all types, while the remainder are type-specific markers. Expression levels are computed by pooling cells from all ages. Representation as in **Figure S1I**.
B. Same as A, for GABAergic types within subclasses (panels, left to right).
C. Same as A, for non-neuronal types.
D. Dot plot showing that type-specific markers for L2/3 glutamatergic neurons vary with age. Also shown are markers for the precursor types AB and BC at P8 and P14, which are expressed in types A, B and C at later ages (P17-P38).
E. Dot plot showing that type-specific markers for L4 glutamatergic neurons also vary with age.
F. Dot plot showing that type-specific markers for L5 glutamatergic neurons are stable with age
G. Dot plot showing that type-specific markers for L6 glutamatergic neurons are stable with age

Figure S4

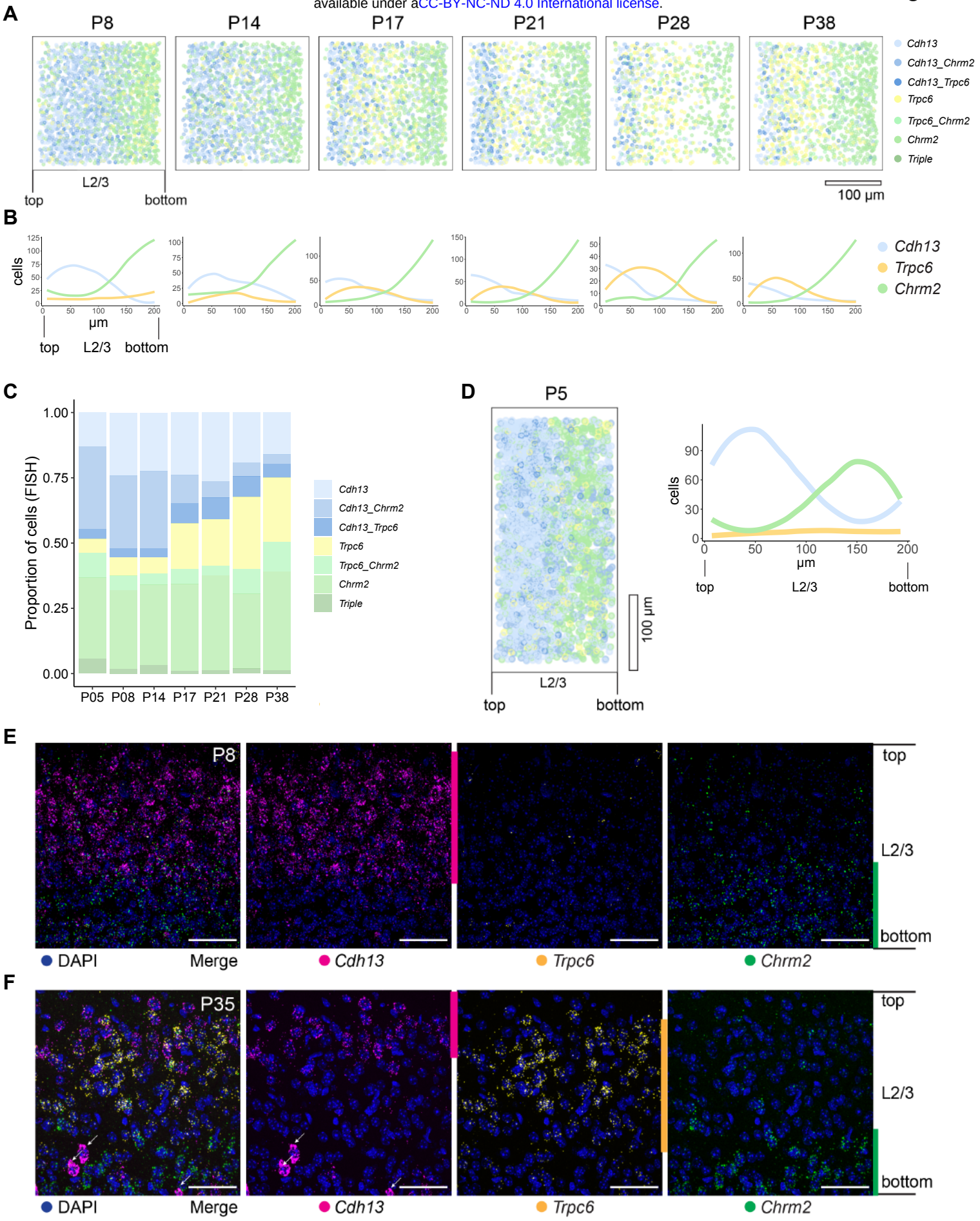

Figure S4. *In situ* analysis of L2/3 glutamatergic neuron types in normally reared mice

A. Pseudo-colored representation of imaged cells (**Methods**) within L2/3 expressing one or more of the type markers *Cdh13, Trpc6,* and *Chrm2* across the six ages. Each panel represents overlaid FISH images of 18 V1 regions from three mice imaged at 40X with the pial-ventricular axis oriented horizontally from left to right. Each imaging frame is 208 µm x 208 µm and is imaged starting at the top of L2/3 to the end of the imaging frame covering about the usual thickness of L2/3 in one frame. As pia could not be imaged within the same frame at 40X, alignment of overlaid images is less optimal compared to 20X images in the main figure. During quantification, this leads to an underrepresentation of *Cdh13*$^{+}$ cells at the top of the imaging frame in 40X compared to 20X images.
B. Line tracings quantifying number of cells per bin at each position along the pial to ventricular axis (x-axis) divided into 14 equally spaced bins, corresponding to panel A. 0 on the x axis is the region of L2/3 closest to pia.
C. Relative proportions of cells within each expression group defined in panel A as quantified by FISH. Total number of cells analyzed: P5, 2106; P8, 3734; P14, 2937; P17, 3102; P21, 2078; P28, 2078; and P38, 2775. Scale bar, 100 µm.
D. Same as panels A and B, at P5.
E. 40X FISH images of L2/3 at P8 labeled with the three type markers *Cdh13*, *Trpc6*, and *Chrm2* that become evident after P17. *Cdh13* and *Chrm2* are selectively expressed between the precursor types AB and BC at earlier ages. *Trpc6* is not expressed at this early stage. Pial to ventricular axis is oriented vertically from top to bottom. Scale bar, 50 µm.
F. 40X FISH images of L2/3 at P35 labeled with the three type markers *Cdh13*, *Trpc6*, and *Chrm2* showing sublayering along the pial to ventricular axis (top to bottom). Arrows denote inhibitory neurons expressing *Cdh13*. Scale bar, 50 µm.

Figure S5

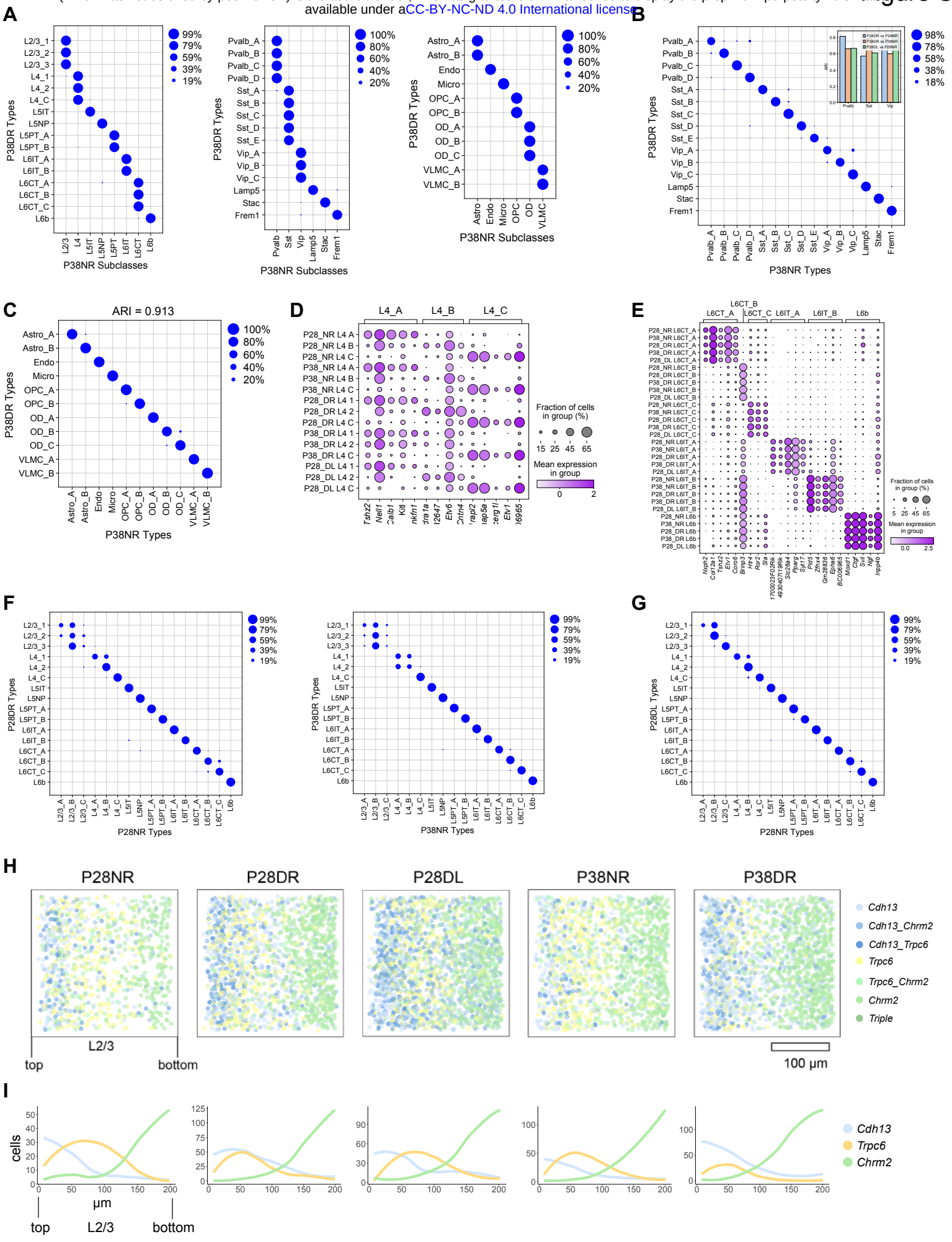

Figure S5. Transcriptomic changes in V1 cell type-diversity in dark-rearing experiments

A. Confusion matrices from supervised classification analyses showing that transcriptomically-defined clusters in dark-reared (DR) mice (rows) map to the correct subclass in normally-reared (NR) mice (columns). This shows that the transcriptome-wide signatures that define the major subclasses are not disrupted by visual deprivation. Panels correspond to glutamatergic (*left*), GABAergic (*middle*) and non-neuronal (*right*) subclasses at P38. Results are similar when comparing P28DR vs. P28NR or P28DL vs. P28NR (data not shown).

B. Confusion matrix from a supervised classification analysis showing that GABAergic clusters in P38DR mice (rows) transcriptomically correspond 1:1 to GABAergic types in P38NR mice (columns). Results are similar when comparing P28DR vs. P28NR and P28DL vs. P28NR (data not shown). Together these results show that the transcriptomic signatures that define types within GABAergic neurons are not disrupted by visual deprivation. Inset, barplot of the adjusted rand index (ARI) showing high transcriptomic correspondence between P28DR, P38DR and P28DL types and NR types at the same age.

C. Same as panel B, showing the 1:1 transcriptomic correspondence of non-neuronal types between P38DR vs P38NR. ARI value is indicated on top. Results are similar for P28DR vs. P28NR and P28DL vs. P28NR (data not shown). Thus, the transcriptomic signatures that define non-neuronal types are not disrupted by visual deprivation.

D. Dot plot showing expression patterns of L4 type markers (columns) in NR types at P28 and P38, and DR and DL clusters at the same ages (rows). Markers are grouped by those specific for NR types L4_A, L4_B and L4_C (annotation bar, top).

E. Same as panel D for L6 types. L6 types in DR and DL experiments show a 1:1 correspondence with the NR types (panels D and E), and are therefore named accordingly. A similar 1:1 mapping is not possible for L2/3 and L4 clusters in DR and DL experiments because of the disruption of type-specific gene expression signatures.

F. Confusion matrices showing the transcriptomic correspondence between glutamatergic clusters in DR vs. types in NR at P28 (left) and P38 (right). Except for the three types in L2/3 and two types in L4, all the remaining types have a 1:1 match with a DR cluster. Thus, visual deprivation selectively impacts type-specification within L2/3 and L4 among glutamatergic types.

G. Confusion matrix showing the transcriptomic correspondence between glutamatergic clusters in DL vs. types in NR at P28. While the patterns are similar to panel D, L2/3 and L4 clusters show an increased correspondence, reflecting partial recovery of cell type specific signatures.

H. Pseudo-colored representation of imaged cells (**Methods**) within L2/3 expressing one or more of the type markers *Cdh13, Trpc6,* and *Chrm2* across five combinations of age and conditions, indicated on top. Each panel represents overlaid FISH images of 15-18 V1 regions from three mice imaged at 40X, with the pial-ventricular axis oriented horizontally from left to right. Each imaging frame is 208 µm x 208 µm and is imaged starting at the top of L2/3 to the end of the imaging frame covering about the usual thickness of L2/3 in one frame.

I. Line tracings quantifying number of cells per bin at each position along the pial to ventricular axis (x-axis), divided into 14 equally spaced bins, corresponding to panel H. 0 on the x-axis is the region of L2/3 closest to pia. Total number of cells analyzed in H, I: P28, 933; P28DR 1671; P28DL, 2148; P38NR, 1419; and P38DR, 1784.

Figure S6

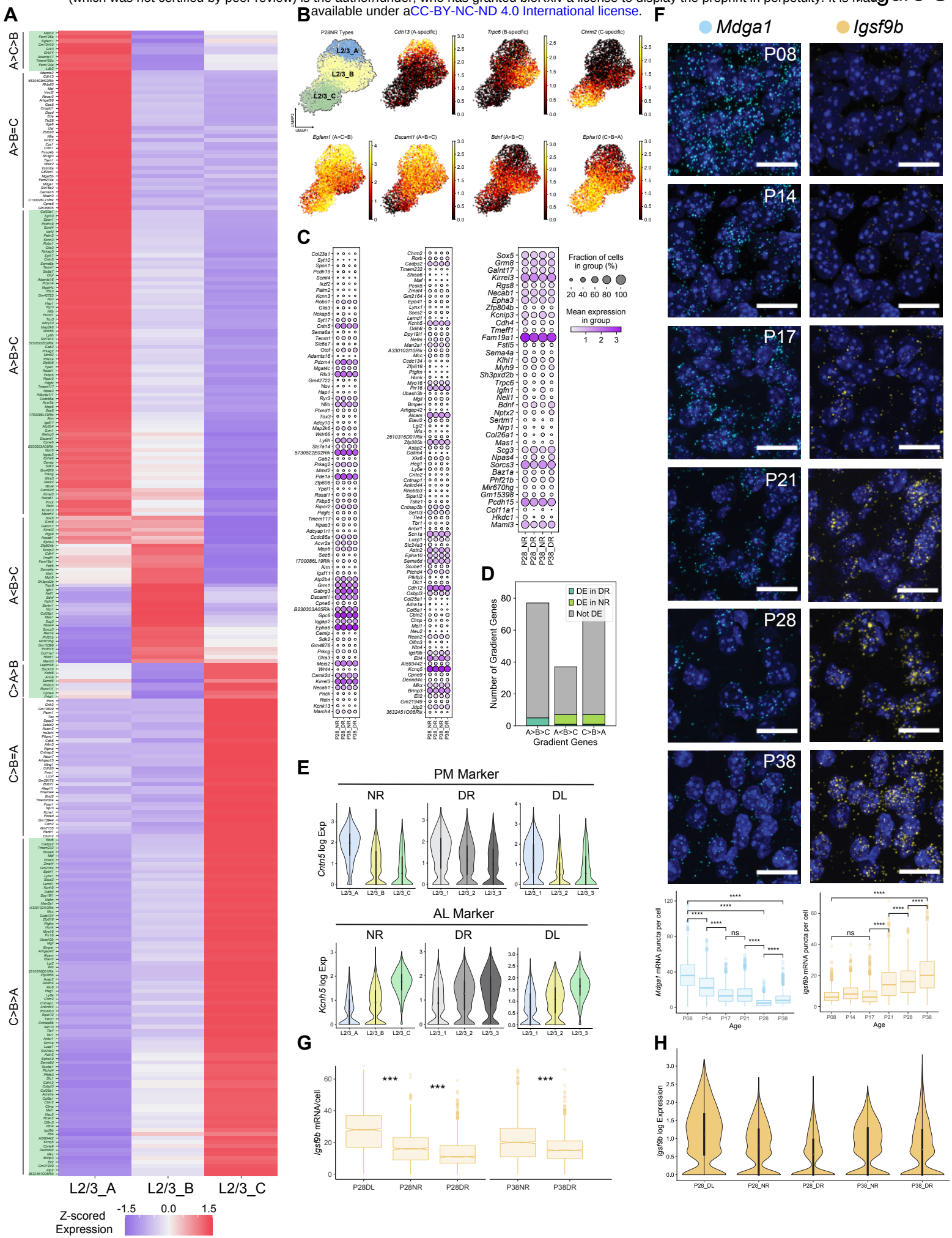

Figure S6. Graded gene expression among L2/3 types and relationship of these patterns to projection specificity and inhibitory synapse regulation

A. Type-specific genes for L2/3 types A, B and C (columns) are predominantly expressed in a graded (i.e., not digital) fashion among the types. Each type was compared to the other two, and only genes with a fold-change (FC) cutoff >2 were selected ($P < 10^{-10}$ by Wilcoxon rank-sum test). Colors denote z-scored expression levels across the three types. Genes (rows) are grouped by expression patterns among the types (e.g., A> B> C). The analysis was performed at P28NR, and the pattern of expression is similar at P38NR (data not shown). Green shading highlights graded genes, which are shown in **Figure 6A**.

B. UMAP feature plots of L2/3 neurons at P28NR with cells colored based on their expression of select DE genes from panel A. The leftmost panel on the top row shows the locations of the three types L2/3_A, L2/3_B, and L2/3_C. The remaining panels on the top row show three genes that are digitally expressed among the three L2/3 types. The bottom panels show four genes expressed in a graded fashion among the three L2/3 types.

C. Dot plots showing that bulk expression levels for most graded genes (as in panel A) are similar between NR and DR conditions at both P28 and P38. Panels correspond to genes in the pattern groups A > B > C (*left*), C > B > A (*middle*) and A < B > C (*right*).

D. Bar plot showing that only a small fraction of graded (shaded) genes from A are differentially expressed when L2/3 cells are compared in bulk between DR and NR mice at P28 (fold-change>2, *P-value* $< 10^{-10}$ by Wilcoxon rank-sum test). Thus, visual deprivation does not change the average expression levels of these genes but disrupts their graded patterning.

E. Violin plots showing expression of markers enriched in PM (top) and AL (bottom) projecting neurons from Kim et al., 2020 in L2/3 cell types in NR mice vs. L2/3 cell clusters in DR and DL mice at P28. The graded expression in NR types is disrupted in DR clusters and partially recovered in DL clusters.

F. (*Top*, *left* and *right*) FISH images showing the expression of *Mdga1* and *Igsf9b* mRNA over time in V1. Three animals per time point, six images per animal. Scale

bar, 20 µm. (*Bottom, left* and *right*) Box plots quantifying expression. Wilcoxon Rank Sum Test, **** p <0.0001. Number of cells quantified: P8,1191; P14,1011; P17, 1389; P21, 1729; P28, 1277; and P38, 1588.

G. Box plot showing quantification of the images in **Figure 6I**. Three animals imaged per age and condition combination. Number of cells quantified: P28NR, 1290 cells; P28DL, 1506 cells; P28DR, 1521 cells; P38NR, 1629 cells; and P38DR, 1885 cells. Quantified at 40X. Wilcoxon Rank Sum Test, *** p <0.001.

H. Violin plot showing expression of *Igsf9b* in snRNA-seq data across the five conditions.

SUPPLEMENTAL TABLES

Table S1. List of canonical markers used to identify neuronal and non-neuronal subclasses.

Table S2. Number of cells present in each of the 18 NR and 9 DR/DL datasets.